Direct Numerical Simulation of Transient Cumulus Cloud Flow

A Thesis

Submitted for the Degree of

Master of Science (Engineering)

by

Prasanth P.

Engineering Mechanics Unit
Jawaharlal Nehru Centre for Advanced Scientific Research
(A Deemed University)
Bangalore – 560 064

JANUARY 2014

To the people affected by the Uttrakhand floods.

DECLARATION

I hereby declare that the matter embodied in the thesis entitled "**Direct Numerical Simulation of Transient Cumulus Cloud Flow**" is the result of investigations carried out by me at the Engineering Mechanics Unit, Jawaharlal Nehru Centre for Advanced Scientific Research, Bangalore, India under the supervision of **Prof. Roddam Narasimha** and **Prof. Suresh Madusudhan Deshpande** and that it has not been submitted elsewhere for the award of any degree or diploma.

In keeping with the general practice in reporting scientific observations, due acknowledgment has been made whenever the work described is based on the findings of other investigators.

Prasanth P.

CERTIFICATE

We hereby certify that the matter embodied in this thesis entitled "**Direct Numerical Simulation of Transient Cumulus Cloud Flow**" has been carried out by Mr Prasanth P. at the Engineering Mechanics Unit, Jawaharlal Nehru Centre for Advanced Scientific Research, Bangalore, India under our supervision and that it has not been submitted elsewhere for the award of any degree or diploma.

Prof. Roddam Narasimha
(Research Supervisor)

Prof. Suresh Madusudhan Deshpande
(Research Supervisor)

Acknowledgements

I would like to thank my advisors Prof. Narasimha and Prof. Deshpande for their constant encouragement and support especially during the last few weeks. I would like to thank Dr. U N Sinha (CMMACS Bangalore) for his help during my visit to CMMACS. I would like to thank Dr.Seshu, CMMACS for letting us use their computational facility. I would like to thank Dr. Sunil Sherlekar and his team from parallel computing labs, Intel Bangalore for their help and support. I would like to thank all my friends at JNC for making my stay at JNC a memorable one. Thanks to Navaneeth, Ponnulakshmi, Srikanth, Saikishan, Anubhab, Sumesh, Deepak, Sourabh Diwan for all the interesting discussions, to Rohith V S and Sharath K Jose for all the fun trips to "Nandini". Special thanks to the JNC football group (Dhiraj Singh, Sunil, Shashank, Rohan Subbiaha, Milind Dhake, Rohith VS , Sharath Jose, Kanwar, Chandradish Ghosh, Piyush, Shreyas etc.). I would like to thank Kanwar, Deepthi, Ponnu, Deepak, Chakri, Milind and Aman for their help in completing my thesis.

Above all, I would like to thank my parents for their unconditional love and support.

Abstract

Clouds play a major role in climate change, and the ability to simulate moist convection patterns is crictical for prediction of tropical weather and climate. Cumulus clouds in particular can play a significant role in transportig heat across the whole extent of the atmosphere. Recent laboratory experiments (Narasimha *et al.* (2011) have successfully reproduced a variety of naturally occurring clouds, and suggest that the transient diabatic plume, subjected to off-source diabatic heating is the appropriate cumulus flow model. In the present work we report the first direct numerical simulation of a transient diabatic plume as a fluid-dynamical model for understanding cumulus flows.

The simulation solves the 3D Navier-Stokes-Boussinesq equuations for an axisymmetric transient diabatic plume. The equations were solved using a fractional step method within the finite volume frame work. The solver developed has been validated against three bechmark cases - (i) lid driven cavity flow; (ii) Rayleigh-Benard convection and (iii) Turbulent-jet simulations. The visualisations of the cloud flow were carried out using a coarse grid of around 4 million grid points, The final simulation was performed using 128 million grid points at a Reynolds number of 2000. The computations were carried out in the ICE cluster housed at CSIR Fourth Paradigm Institute, Bangalore.

As on date only one realisation of the flow has been carried out. The inferences drawn are therefore subject to certain statistical fluctuations. Nevertheless, the results show that the forms of the flows generated resemble naturally occurring cumulus clouds. The variation of the width of the flow with height towards the end of the simulations shows 5 distinct regimes - 1. a nearly laminar constant width regime; 2. a nearly linearly growing turbulent plume regime; 3. the heat injection zone where the width is nearly constant with height; 4. a regime of slow growth in width culminating at a maximum and 5. a short dome like cloud top. Apart from the distribution of the flow width, those of maximum velocity in the plume and total mass flow across it at each section has been evaluated. Because the simulation provides complete vorticity field, it is possible to obtain the mass flow across the plume area bounded by a well defined vorticity edge of the plume. Entrainment coefficients involving the complete mass flow in the turbulent vortical region of the plume have therefore become possible for the first time. Using smoothed fields a preliminary estimate of the entrainment coefficient as it varies with height and in time is

presented. The development of the code for the transient diabatic plume enables us to obtain more precise statistical estimates by ensemble averaging. This is a task that can now be completed if adequate computer resources are available, and will be part of future work.

List of Figures

List of Tables

Contents

Chapter 1
Introduction

Clouds have fascinated man for several centuries. Poets and artists fascinated by their beauty have used them in their works extensively (e.g. Meghaduta by Kalidasa). In the modern day, they have been a subject of interest to meteorologists across the globe due to their profound influence on climate change and global warming. Clouds are one of the least understood domains in climate sciences and are listed in the most urgent problems requiring attention by the Intergovernmental Panel on Climate Change (Randall *et al.* (2007)). According to one estimate (Ramaswamy *et al.* (2001)) a 5% increase in short wave cloud forcing would be sufficient to wipe out all the effects of the green house gases emitted between 1750 and 2000. Clouds are an example of a flow system with complex interactions among microphysics (multiphase fluid flow, thermodynamics and phase transition) , flow turbulence and radiation, and to this date remain a challenge to researchers.

A cloud is defined as "a visible aggregate of minute particles of water or ice or both in the free air"(Houze Jr (1994). Clouds exhibit a wide variety of shapes and sizes, and each type plays a different role in the global atmospheric circulation. Clouds are classified based on a nomenclature developed by Luke Howard, a British chemist and amateur meteorologist (Narasimha (2012)). Of all the cloud species, the most interesting are the type called cumulus (Latin word for "heap" or "pile"), because of their scientific importance and distinct shapes. Cumulus clouds (figure 1.1) are defined as "detached clouds, generally dense and with sharp outlines, developing vertically in the form of rising mounds, domes or towers, of which the bulging upper part often resembles a cauliflower" (Houze Jr (1994)). Clouds have a lifespan that ranges range from the order of a few minutes to almost a day in the case of large scale systems (Narasimha (2012)), and are unsteady throughout their evolution. Cumulus clouds play a major role in tropical convection. They have a flat base and can rise to a height of 15km or more. These tower-like structures can transport heat across the whole vertical extent of the atmosphere (Narasimha (2012)). Present-day cloud models have not been able to account for the effects of clouds satisfactorily, particularly in the tropics. Accurate predictions of rainfall are important for tropical countries. Particularly in a country like India, the accurate prediction of the monsoons can have a significant impact on the economy of the country; in fact a Union Finance Minister of India called the Indian monsoon the "real Finance Minister"(Hindustan Times

2012). Charney & Shukla. (1981) suggest that the predictability in the tropics ought to be greater than in the higher latitudes. But this potential predictability is yet to be exploited because the system is dominated by moist convection, for which existing parameterization schemes are inadequate. For instance, present-day long-range forecasts with existing models have consistently failed to predict the Indian monsoons satisfactorily.

Cumulus cloud formation generally begins with moist air rising up on the slopes of a hill or a mountain or in the form of a plume from a hot patch on the surface of the earth. As the air ascends the temperature drops due to adiabatic expansion. At some height the ascending air is saturated with respect to water vapour. Further ascent reduces the temperature and results in the formation of water droplets and ice crystals from the excess water vapour. The phase transition releases latent heat into the system. The latent heat released increases the buoyancy locally, and this aids in further ascent. This heat release plays a significant role in determining the shape and size of the cloud. These complexities have restricted the number of laboratory simulations of clouds. Until recently most research in clouds was dependent on field measurements, and so the statistics obtained were not conclusive enough as clouds are intermittent in space and time (Narasimha (2012)). A major area of concern in a cumulus cloud is entrainment characteristics, as these determine the major features of a cloud. Entrainment with respect to a cloud is a measure of the amount of ambient dry air entering into an active cloud flow. The rate of ascent and dilution, and the shape of the cumulus cloud, are predominantly dependent on the entrainment characteristics. So capturing the entrainment correctly holds a central position in the study of cumulus clouds.

1.1 Early Entrainment Models

The controversy on the appropriate entrainment model for clouds started in the late 1940's. Numerous models have since been proposed. A comprehensive review on the early entrainment models is presented by Reuter (1986). The issue was first addressed by Stommel in 1947 (Stommel (1947)); he stated that the cloud entrains dry air laterally from its surroundings. Thereafter, measurements made by Byers & Braham (1949) and Starr Malkus (1954) concluded that the theory of lateral entrainment is adequate. In the meanwhile, the idea of thermals (point sources of buoyancy) as an appropriate model for cumulus clouds was proposed by Ludlam *et al.* (1957). The idea that lateral entrainment is unimportant, whereas cloud top entrainment was significant, was first proposed by Warner (1955). Turner (1963),Turner (1983) had proposed various models, which included one based on a solution of Hill's spherical vortex, thermals, similarity plumes, and a starting plume (fig 1.2 A-C). The measurements made by Sloss (1967) suggested that

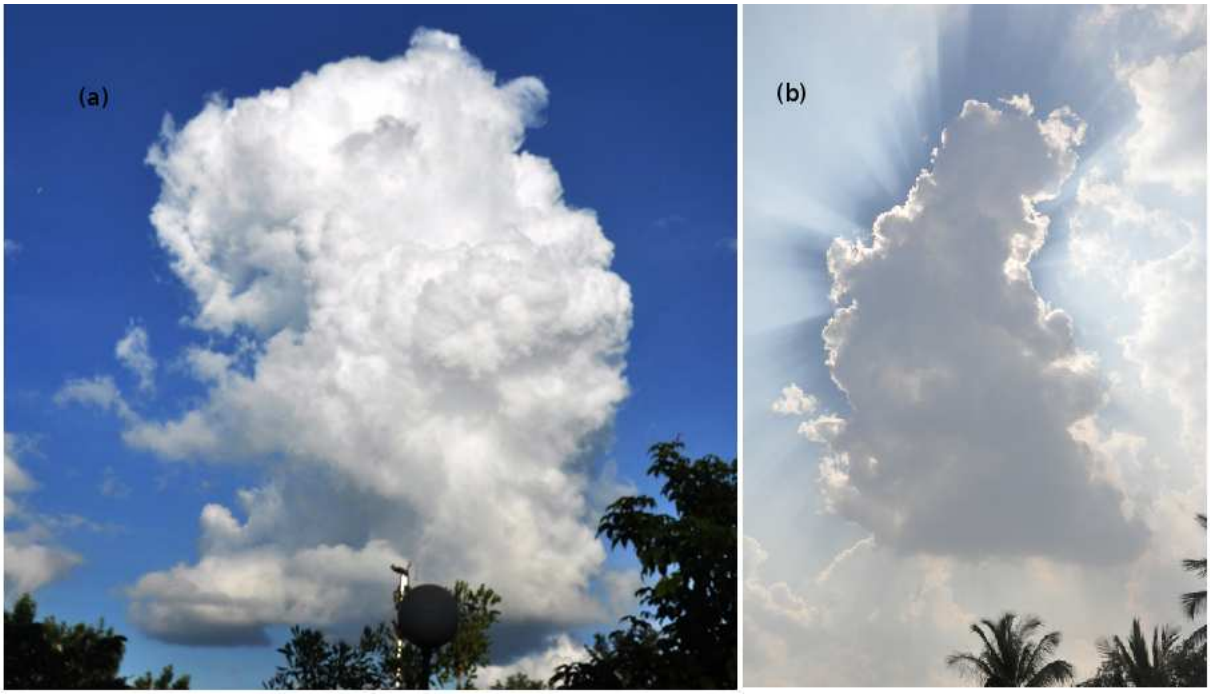

Figure 1.1: Two typical cumulus cloud shapes: (a) Fluffy; (b) Tower-like formation. (Image courtesy: Vybhav G. Rao, EMU, JNCASR)

lateral-entrainment theory was not appropriate. A detailed study conducted by Heymsfield *et al.* (1978), as part of the National Hail Research Experiment (NHRE), confirmed the existence of undiluted moist-adiabatic cores on the upstream side of most cumulus clouds, and observed significant mixing further downstream. An analysis of NHRE data by Paluch (1979) suggested that most of the entrainment occurred far above the observational level, and that the dilution occurred mainly due to the penetrative downdraft mechanism. Analysis showed that the lateral entrainment in these tall clouds may be small as the observed properties can be explained only if air from the cloud base ascends to the top without laterally mixing with the ambient.

These observations discredited the classical lateral entrainment hypothesis proposed by G I Taylor (Taylor (1946)) in a war-time report. The hypothesis states that the mean inflow velocity entraining into a turbulent free shear flow is proportional to a local characteristic velocity scale. This hypothesis is based on the similarity assumption. This model was successful in predicting the entrainment in several practical flows like classical plumes and jets with and without stratification (Morton *et al.* (1956)). This entrainment model, when applied to cumulus clouds, underestimates the height of vertical ascent due to higher dilution as a consequence of over-predicted ambient entrainment.

Flow models have also been proposed based on episodic vertical mixing and shedding thermals (Blyth (1993)). These were later found to explain only flow properties close to

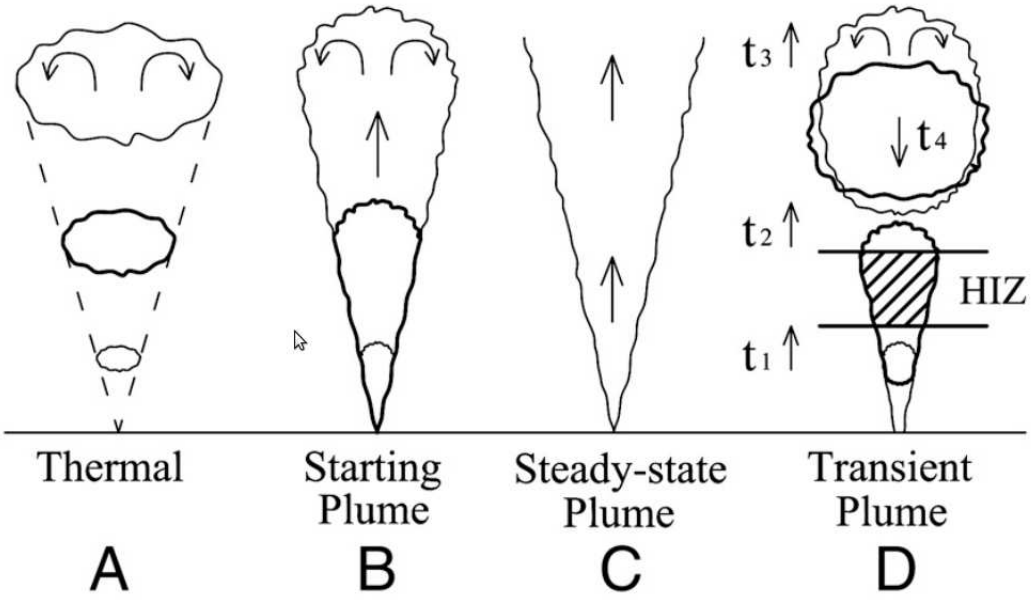

Figure 1.2: Schematic of different physical models for cumulus-cloud evolution with time. Arrows inside the the flow indicate the direction of mean motion relative to plume head. Narasimha *et al.* (2011)

the cloud-top. Some recent studies have shown that the entrainment rates in a cloud are high at the cloud base and drop significantly with altitude (Romps & Kuang (2010)). This observation was not explained by any of the above mentioned entrainment models.

1.2 Appropriate Cumulus Flow Model

Based on the extensive field experiments conducted, a broad schematic picture of cumulus clouds is now available. But until recently, the flow models (mathematical and physical) formulated for a cumulus cloud failed to describe the flow correctly. Several experiments were conducted to reproduce clouds in laboratory conditions. Most of these studies were directed towards understanding small-scale dynamics (Warhaft (2009)). Interesting attempts were made by Turner (1963) where the evolution of bubbles was tracked with their volume increasing with time. But all these attempts failed to shed light on the special features of a cumulus cloud. None of these flow models was able to capture the macrodynamics of cumulus clouds. Recent experiments (Narasimha *et al.* (2011)) have successfully reproduced a variety of naturally occurring cumulus clouds and were able to track their entire history. The experimental setup and its details are discussed by Bhat *et al.* (1989). Based on new experiments "the transient plume subjected to off-source diabatic heating" (fig 1.2 D) is considered as the appropriate flow model for non-precipitating cumulus cloud flows (Narasimha *et al.* (2011)). Two interesting cumulus cloud examples,

simulated experimentally using this flow model and shown in figure 1.3, demonstrate that this model can capture several features of a cumulus flow. Off-source volumetric heating, dynamically scaled to mimic the latent heat release due to phase transition in clouds, plays a significant role in determining the dynamics of the clouds. The variation of the heating profile in both space and time plays a crucial role in determining the shapes of the cloud flow. This flow model captures the inherent transient and non self-similar behaviour of the turbulent cloud flow (Narasimha *et al.* (2011)).

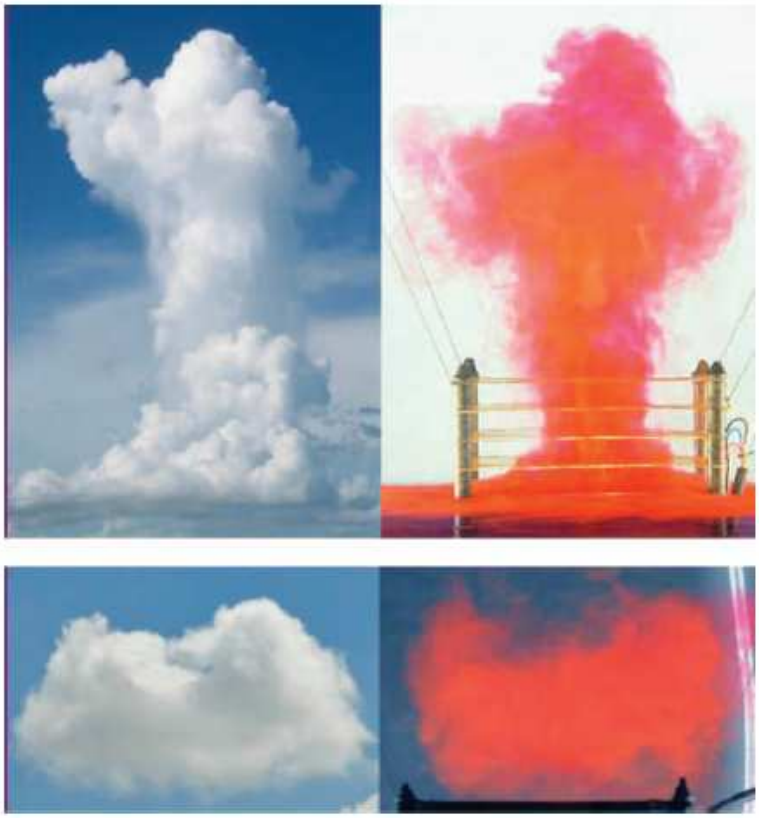

Figure 1.3: Two matched pairs of natural cloud (left) and laboratory experiments (right). (Narasimha *et al.* (2011))

1.3 Previous Studies

The present flow model is an extension of experiments conducted to study the effect of off-source buoyancy in a round jet (Bhat & Narasimha (1996)) and a round plume (Venkatakrishnan *et al.* (1998)). A comprehensive review of the data from these works is presented by Narasimha (2012) and Diwan *et al.* (2011). The results presented in these works are based on steady state measurements as opposed to a transient plume model. But the insights gained from these studies help in understanding the "anomalous entrainment" behaviour in a cumulus cloud flow. Bhat & Narasimha (1996) showed that entrainment coefficient in a heated jet does not follow Taylor's entrainment hypothesis.

The Laser Induced Fluorescence (LIF) images (Venkatakrishnan *et al.* (1998)) show the dramatic effect of heat addition on the structure of the flow. The coherent structures in the flow were disrupted due to the off source heating. The tongue-like structures protruding from the core flow in case of a pure plume or jet were absent when the flow was subjected to off-source heat, and the spread rate of the flow above the heat injection zone underwent drastic reduction. The core flow is well mixed with hardly any trace of ambient fluid, which is very similar to the undiluted protective cores observed in cumulus clouds (Riehl & Malkus (1958)). Similar investigations were carried out by Agrawal *et al.* (2004) and Venkatakrishnan *et al.* (2003), and similar observations were reported. A detailed comparison of the data is given in Diwan *et al.* (2011).

Laboratory experiments have limitations in acquiring all the spatial and temporal flow field information. This limitation can be overcome in case of a numerical experiment. Basu & Narasimha (1999) simulated a temporally evolving heated jet using the Boussinesq assumptions as an analogue of the spatially developing flow in the laboratory. The observations were consistent with the experiments. A dramatic increase in the vorticity was observed post heat injection, and the entraining flow field was altered a great deal due to the distortion of coherent structures. Spatial simulations were conducted by Agrawal *et al.* (2005), but the non dimensional heat release number (sec: 2.3), an important simulation parameter, was 40 times higher than the available experimental results and so a direct comparison is not possible. Konduri (2009) explored the possibility of studying the dynamics of a cumulus flow by performing a DNS of a starting plume subjected to additional off-source buoyancy.

A key objective in all the experiments and the numerical simulations has been to see the effect of off-source heat release on entrainment. Figure 1.4, replotted from Narasimha (2012), shows the variation in entrainment coefficient with height from the cloud base for each laboratory experiment. The data exhibit a trend very different from steady state plumes, thermals and other proposed models. There is a mild increase in the entrainment level just above the cloud base till it peaks and subsequently falls to a value less than the one predicted by similarity theory. These results are broadly consistent with observations in real clouds Narasimha (2012). A detailed review of the results is given in Diwan *et al.* (2011). A mechanism has been proposed based on which the coherent structures are disrupted above the heat injection zone, thus disabling the first step (engulfment) in the entrainment process Narasimha *et al.* (2011). From experiments on free shear flows it was proposed that entrainment is a three step process namely engulfment, mingling and molecular mixing (Brown & Roshko (1974)). The role played by the baroclinic torque, proportional to $\mathbf{g} \times \nabla T$, in the vorticity equation is discussed by Narasimha (2012). The heating generates a mean baroclinic torque which peaks radially midway between the flow

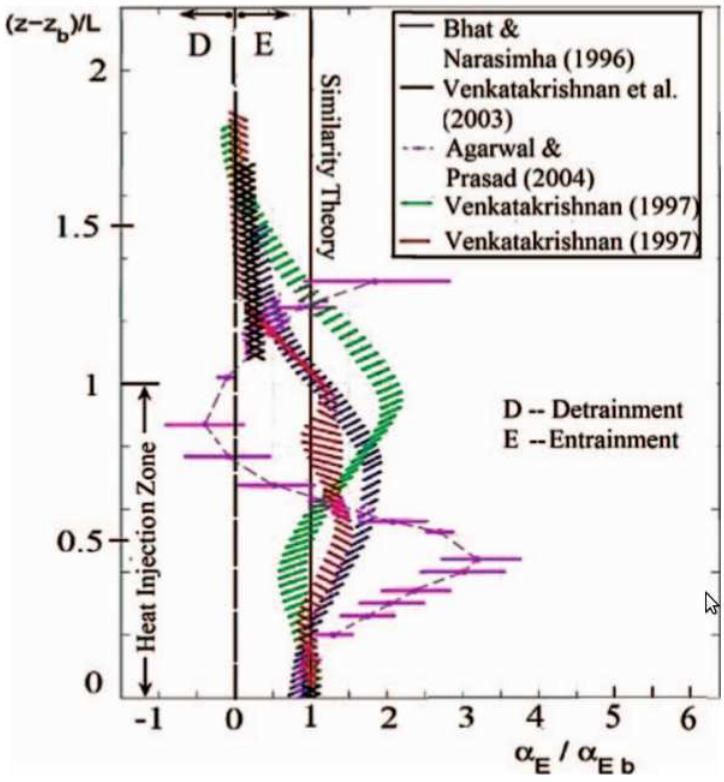

Figure 1.4: Normalized entrainment coefficient data from the experiments on jets and plumes till date. Narasimha (2012)

axis and the lateral edges (on a roughly cylindrical sheet). The sign of the torque acting is such that it enhances the axial velocity at the centre and depresses it at the edges. The engulfment tongues at the edge of the flow are thus folded down and the flow thins down due to enhanced shear. The core of the flow is well mixed, presumably due to the explosive growth of turbulent enstrophy at the smaller scales.

With the advent of faster computers in the 1990s Large Eddy Simulation (LES) of clouds shot to prominence. A detailed review is given by de Rooy *et al.* (2012). LES is a powerful tool in obtaining the quantitative entrainment behaviour of clouds (Siebesma & Cuijpers (1995) and De Rooy & Siebesma (2008)). LES studies have revived interest in the long-standing question of entrainment and detrainment profiles in cumulus clouds. Several studies of shallow cumulus clouds reveal that the detrainment (negative entrainment) profiles vary much more than the entrainment profiles do (De Rooy & Siebesma (2008)). LES studies have been able to reveal a subsiding shell outside the zone of lateral mixing (Jonker *et al.* (2008)). The simulation by Heus & Jonker (2008) shows that entrainment from the lateral direction plays a more significant role than the entrainment from the top in diluting the cloudy updraught, thus contradicting the conclusions by Squires (1958) and Paluch (1979). The observations reported in the study reproduce the Paluch mixing lines (Heus & Jonker (2008)) and track the origin of entrained dry air

by using Lagrangian particles. They concluded that hardly any dry air entrained from the cloud top penetrates downwards to dilute the cloudy updraft. Recent simulations have been able to shed some light on the dynamics of deep convection. Romps & Kuang (2010) reported an LES based on a fully compressible cloud-resolving model with the objective of studying steady state moist convection. They have been successful in estimating entrainment directly by tracking the dilution rate of passive scalars released at the cloud base (Romps & Kuang (2010)). These techniques have been able to provide information on the locally varying entrainment and detrainment coefficients. Recently, Pauluis & Schumacher (2011) simulated conditionally unstable moist convection in the Rayleigh-Benard problem. They incorporated models to account for the thermodynamics and phase transitions in the clouds.

In the present work, we report a Direct Numerical Simulation (DNS) of a transient diabatic plume to study the features of a cumulus cloud flow. A quantitative study on the effect of off-source heat release on the entrainment coefficient is reported here. The rest of the thesis is organised as follows: chapter 2 describes the governing equations and the numerical method implemented. In chapter 3, the DNS solver developed is validated with some standard test cases. The results obtained are discussed in chapter 4. Chapter 5 concludes the present work.

Chapter 2
Numerical details

2.1 Introduction

A numerical approach to the study of any turbulent flow (including cumulus clouds) can be classified into three broad categories: Reynolds Averaged Navier-Stokes (RANS), Large Eddy Simulation (LES) and Direct Numerical Simulation (DNS). Among these only DNS has the capability to provide a complete description of the structure of the flow without appeal to anything beyond first principles, and hence is the most powerful and credible numerical tool in the study of turbulent flows. In particular all the relevant spatial and temporal scales are resolved. DNS is compute-intensive and requires state of the art computing facilities to simulate a physically realistic flow.

With the advent of powerful computing resources, DNS has transformed the approach to understanding turbulent flows at bulk Reynolds numbers of order $10^3 - 10^4$. An interesting review of DNS as a research tool is given in Moin & Mahesh (1998). To capture faithfully the multiscale character of turbulent flow sufficient care has to be taken while discretising the nonlinear governing equations. Unlike in RANS simulations where upwind schemes have been used extensively to make the solver robust, to do DNS a non-dissipative and robust scheme is required. Due to their dissipative nature upwind schemes, with a numerical viscosity that may mask the effects of molecular viscosity, are not widely used for DNS.

It has been observed that improper discretisation of the advective term in the Navier-Stokes equations will lead to numerical instability at a higher Reynolds number. The non-linear terms computed in physical space can result in aliasing errors which in turn can trigger numerical instability. Arakawa (1966) showed that for long-time numerical integration of two-dimensional flows using a vorticity-stream function formulation, conservation of enstrophy in the absence of physical or numerical viscosity is important. In the velocity-pressure formulation, the corresponding higher order variable is kinetic energy. Morinishi *et al.* (1998) showed that the discretisation of the advective term in the momentum equation should conserve kinetic energy to ensure numerical stability and non-dissipative behaviour. Verstappen & Veldman (2002) extended the idea of kinetic energy

conservation in a discrete sense to non-uniform grids, and Mahesh *et al.* (2004) used these ideas to develop an algorithm for performing DNS and LES of incompressible flows in an unstructured frame work. Discrete conservation of mass, momentum and kinetic energy ensures the robustness of the solution procedure without the use of numerical/artificial viscosity.

2.2 Governing Equations

From the evidence of the laboratory experiments of Narasimha *et al.* (2011) and previous numerical simulations (Basu & Narasimha (1999), Konduri (2009)), the dynamics of the flow can be considered to be essentially incompressible and the effect of variation of density appears only as a source term in the momentum equation. So, the Boussinesq approximation may be used to simplify the compressible Navier-Stokes equations, the density differences being neglected except when they are coupled with the accleration due to gravity in the momentum equation (Spiegel & Veronis (1960)). This is equivalent to saying that the buoyancy force is comparable with the inertia force in the limit of small density differences because the flow acceleration is small compared to acceleration due to gravity. The off-source heat injected into the flow appears as a source term in the temperature transport equation as given in Basu & Narasimha (1999). The governing equations with off-source heat addition (which may be called the diabatic Boussinesq equations) are

Continuity equation:

$$\nabla \cdot \boldsymbol{u} = 0, \tag{2.1}$$

Momentum equation:

$$\partial_t \boldsymbol{u} + (\boldsymbol{u} \cdot \nabla)\boldsymbol{u} = -\frac{1}{\rho}\nabla p + \nu \nabla^2 \boldsymbol{u} - \boldsymbol{g}\alpha T, \tag{2.2}$$

Energy equation:

$$\partial_t T + (\boldsymbol{u} \cdot \nabla)T = k\nabla^2 T + \frac{J(t)}{\rho c_p} H(x, y, z, t), \tag{2.3}$$

where $\boldsymbol{u}$ is the velocity vector, T is the change in temperature above the ambient, p is the pressure, ρ is the ambient density, c_p is the specific heat at constant pressure, ν is the kinematic viscosity, k is the thermal conductivity, α the coefficient of thermal expansion, $\boldsymbol{g}$ is the acceleration due to gravity acting vertically downwards, $J(t)$ is the heat added per unit volume per unit time as a function of time and $H(x, y, z, t)$ is the heat distribution function which determines the spatial zone within which the heat is released.

2.3 Non-dimensionalisation

For the cloud flow, the hot patch diameter d_o is chosen as the length scale and its temperature differential above the ambient, T_o, is chosen as the temperature scale. The velocity scale is obtained as $U_o = \sqrt{g\alpha d_o T_o}$. These scales are used to non-dimensionalise the governing equations given in the previous section. The non-dimensional equations so obtained are

$$\nabla^* \cdot \mathbf{u}^* = 0, \tag{2.4}$$

$$\partial_t^* \mathbf{u}^* + \mathbf{u}^*.\nabla^* \mathbf{u}^* = -\nabla^* p^* + \frac{1}{\mathrm{Re}} \nabla^{*2} \mathbf{u}^* + T^* \hat{z}, \tag{2.5}$$

$$\partial_t^* T^* + \mathbf{u}^*.\nabla^* T^* = \frac{1}{\mathrm{Re\ Pr}} \nabla^{*2} \mathbf{T}^* + G(t) H(x, y, z, t), \tag{2.6}$$

where, the starred quantities represent the non-dimensional variables. The three non-dimensional numbers are:

$$Reynoldsnumber, Re = \frac{U_o d_o}{\nu} \tag{2.7}$$

$$Prandtlnumber, Pr = \frac{\nu}{k} \tag{2.8}$$

$$Heatreleasenumber, G = \frac{J}{\rho c_p} \frac{d_o}{U_o T_o} \tag{2.9}$$

For convenience, the asterisk (*) will be dropped from the non-dimensional terms in the following.

2.4 Time discretisation

Due to the presence of multiple time scales, turbulent flows are categorised as a stiff system with respect to time advancement (Moin & Mahesh (1998)). To capture the smaller scales accurately smaller time steps are required. So, an implicit time integration scheme may not be required for lower Reynolds number and Prandtl number. For the simulations presented here, second order Adams-Bashforth discretisation has been used for the nonlinear and the viscous terms. The pressure and buoyancy terms are treated implicitly.

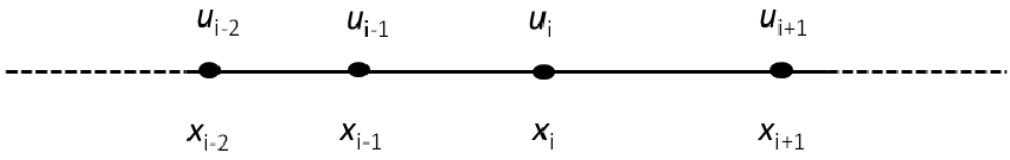

Figure 2.1: 1D non uniform grid

2.5 Spatial discretisation

As mentioned previously, conservation of mass, momentum and kinetic energy in the discrete system plays a significant role in ensuring the accuracy and robustness that are essential for DNS of turbulent flows. Morinishi *et al.* (1998) have discussed the conservation properties of schemes for incompressible Navier-Stokes equations on a uniform grid. Verstappen & Veldman (2002) extended the formulation to account for symmetry preservation in a non uniform grid. In the present simulations symmetry-preserving, kinetic energy conserving discretisation is used in a nonuniform cartesian grid. For example, the first and second derivatives on a 1D grid (figure 2.1) are given by

$$\partial_x u(x_i) = \frac{u_{i+1} - u_{i-1}}{x_{i+1} - x_{i-1}} \tag{2.10}$$

$$\partial_{xx} u(x_i) = [\frac{u_{i+1} - u_i}{x_{i+1} - x_i} - \frac{u_i - u_{i-1}}{x_i - x_{i-1}}] \frac{2}{(x_{i+1} - x_{i-1})} \tag{2.11}$$

An important point to be noted here is that the skew symmetry of the advective operator is preserved at the expense of the local truncation error. In a nonuniform grid the local truncation error is $O(\Delta x)$, which is not of much significance as the global error is $O(\Delta x^2)$ (Verstappen & Veldman (2002)).

2.6 Solution Algorithm

In the incompressible Navier-Stokes equations, the velocity and pressure fields are strongly coupled and the continuity equation has no time derivative. Mass conservation has therefore to be enforced implicitly through the pressure field in the momentum equation. This difficulty can be eliminated in a 2D case where a vorticity-streamfunction formulation can be used, but for a 3D system there is no option but to work with the primitive variables. In the late 1960's Chorin (1968) and Temam (1969) introduced the idea of fractional-step/projection methods to solve the incompressible Navier-Stokes equations in the primitive variable form, and the methods have since then emerged as a separate topic of research.

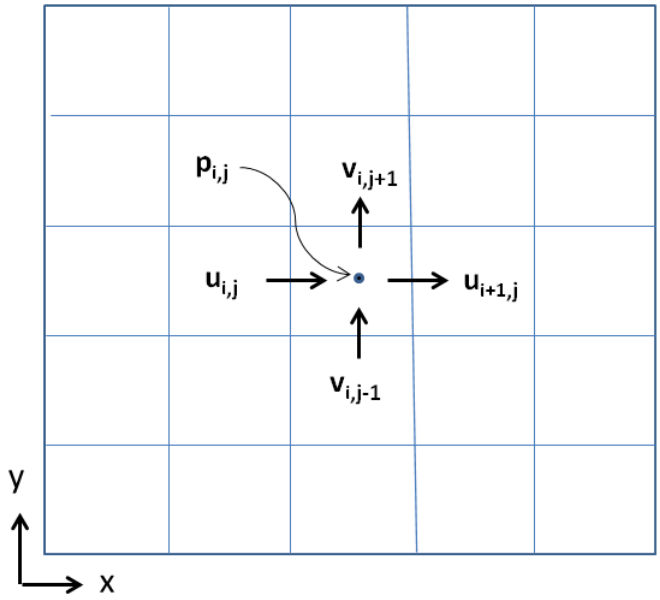

Figure 2.2: 2D staggered grid

For the simulations presented here, a fractional-step/time-split method is used within a finite volume framework. The primitive variables are stored in a staggered format(figure 2.2). The pressure (p) is stored at the cell centre and the velocities (u_i) are stored at the cell faces. A non-uniform cartesian grid layout (figure 2.3) is used to provide adequate resolution in the core flow region.

In the first step of the solution procedure, a pseudo-velocity field ($\hat{u}_i$) is calculated from the non-linear (NL), viscous ($VISC$) and buoyancy terms in the momentum equation. In the following step, the pseudo-velocity field which does not satisfy the divergence-free criterion locally is projected into a divergence free space through the projection operator. The steps in the algorithm are given below.

Step1:

$$\frac{\hat{\boldsymbol{u}}_{\boldsymbol{i}} - \boldsymbol{u}_{\boldsymbol{i}}^{\boldsymbol{n}}}{\Delta t} = \frac{1}{2}[3(-NL + VISC)^n - (-NL + VISC)^{n-1}] + T^{n+1}\hat{z} \tag{2.12}$$

Step2:

$$\frac{u_i^{n+1} - \hat{u}_i}{\Delta t} = -\frac{\partial p^{n+1}}{\partial x_i} \tag{2.13}$$

The pseudo velocity obtained from equation 2.12 is used to obtain the correct velocity field ($\boldsymbol{u}^{n+1}$). Taking divergence of equation 2.13 and using the mass conservation equation gives the Poisson equation for the pressure field (2.14),

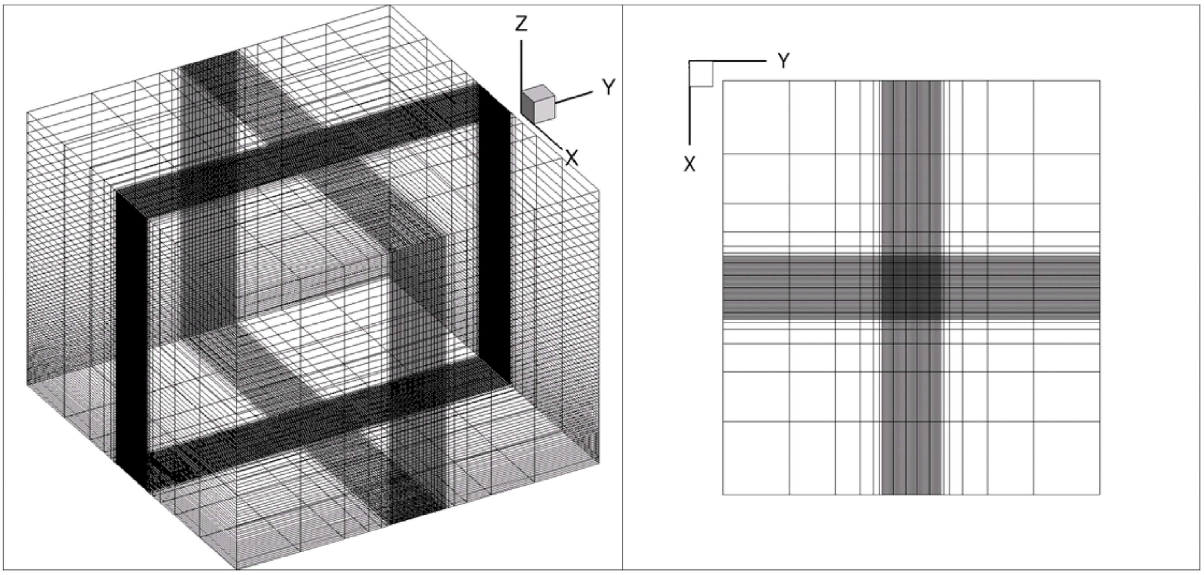

Figure 2.3: Non-uniform cartesian grid

$$\nabla^2 p^{n+1} = \frac{\nabla \cdot \hat{\boldsymbol{u}}_{\boldsymbol{i}}}{\Delta t} \tag{2.14}$$

The resulting pressure field is correct $O(\Delta t)$. The divergence-free velocity field ($\boldsymbol{u^{n+1}}$) is obtained by correcting the pseudo velocity field using the gradient of the pressure field obtained from equation 2.14. The velocity field obtained is correct $O(\Delta t^2)$. The details of the order of accuracy are discussed in Perot (1993).

2.7 Scalar equation

The numerical integration of a scalar equation is different from the momentum equation in the incompressible Navier-Stokes equations. The pressure term in the momentum equation, coupled with the divergence free criterion, does not permit sharp gradients in the velocity field (Muppidi & Mahesh (2008)). The absence of a pressure-like term in the scalar equation can produce gradients sharper than in the velocity field even when the Schmidt number (Sc) is 1. This can pose numerical constraints on the time step size and the sharp gradients can trigger dispersive errors. The governing equation for a scalar C can be written as follows

$$\partial_t C + \nabla \cdot (C\boldsymbol{u}) = \frac{1}{\text{Re Sc}} \nabla^2 C + \text{source} \tag{2.15}$$

In the simulations presented in this thesis two scalars are used. One of them is the

active scalar temperature, and the other a passive scalar analogous to dye concentration in the laboratory experiment. The Prandtl number (Pr) and Schmidt number (Sc) used in the simulations are unity to prevent severe restrictions on the size of the time step.

The scalar system considered here has sharp gradients and so a higher order advection scheme will introduce numerical oscillations (dispersive errors) into the system in the vicinity of discontinuities. This would affect the boundedness of the scalar field. On the other hand, a first order upwind scheme preserves boundedness but introduces numerical diffusion and smears out the sharp gradients. To preserve the boundedness property a simple predictor-corrector technique, introduced by Herrmann *et al.* (2004), is implemented. In the predictor step, the scalar equation is integrated using the higher order discretisation scheme (2nd order central differencing in this case). If the scalar value is out of bounds at any grid point, then in the corrector step the higher order discretisation in the predictor step is replaced locally with a first order upwind stencil. So the scheme is diffusive only in the region having sharp gradients. This scheme is very simple to implement and is also computationally very efficient.

2.8 Boundary Conditions

A mathematical model of any physical system is incomplete without the appropriate boundary conditions. In the case of the Navier-Stokes-Boussinesq equations, boundary conditions are required for the velocity vector, pressure and temperature. Specifying consistent boundary conditions in a strongly coupled velocity-pressure field is difficult because of finite domain size (truncation of the computational domain from the rest of the universe). Inappropriate boundary conditions can trigger non-physical oscillations which can corrupt the solution field. The most difficult boundary condition is the one where the flow leaves the boundary. The conditions specified on these boundaries are called outflow boundary conditions (OBC). A consistent OBC is tractable in case of simple laminar flows by pushing the outflow boundary downstream. This idea is computationally very expensive in the case of DNS of turbulent flows. The objective of a good outflow boundary condition is to reduce the upstream effect and allow the flow to exit the domain gracefully (Sani & Gresho (1994)).

For the cloud flow, the bottom plane is treated as a no-slip wall with a hot circular patch at the centre. The lateral boundaries are treated as no slip adiabatic walls. At the top boundary, the normal derivatives of all the variables are set to zero except pressure; the pressure boundary condition is motivated from the continuity equation and is taken as

$$\frac{\partial p}{\partial n} = -\frac{\delta}{\Delta t} \tag{2.16}$$

where,

$$\delta = -\frac{1}{S_N}\int_S (\boldsymbol{n}\cdot\hat{\boldsymbol{u}})dS \tag{2.17}$$

where S_N is the surface area in the normal direction at the outflow boundary, S is the surface of the computational domain and S_N is the area of the outflow boundary. Further details are given in Sani & Gresho (1994).

2.9 Linear Algebra Solver

Solving elliptic equations numerically is a computationally expensive task. Traditional iterative schemes have very slow convergence due to the slow damping of the lower wavenumbers. Efficiency of the elliptic linear system solver dictates the computational efficieny of the incompressible Navier-Stokes solver. The pressure in the incompressible flow is governed by the elliptic Poisson equation, the source term having contributions from the non-linear and buoyancy terms in the momentum equation.

A wide variety of efficient algorithms exist to solve the linear system obtained from the discretisation of a Poisson equation. The efficiency of each of these algorithms varies depending on the nature of the grid/stencil and the number of unknowns. For instance, a Fourier-based method coupled with a tridiagonal matrix solver is one of the best combinations to solve a 3D problem with at least two periodic directions. But this method cannot be used if the grid is non-uniform in at least two directions. In such a situation, the best option is to use an iterative solver within a multigrid framework.

A multigrid based algorithm can give a grid-independent convergence and is the most general and efficient iterative technique to solve a sparse linear system of equations. The multigrid frame work consists of two fundamental components namely, error smoothing and coarse grid correction. Iterative schemes like Gauss-Siedel and Gauss-Jacobi, commonly known as relaxation schemes, have slow convergence due to the inefficient damping of the low frequency errors. Eigenvalue analysis of the iterative method reveals that the error components belonging to the low frequencies have an amplification value close to 1 and so they converge very slowly. But the higher frequencies are damped effectively. In a multigrid framework, the relaxation schemes are good smoothers. A few sweeps of any of these relaxation schemes will smoothen the residue which can be restricted onto a coarser grid. The low frequency errors in a refined mesh progressively approach higher frequencies (relatively) as they are projected onto a coarser grid. At each grid level the high frequencies are damped by the iterative scheme. In a nutshell, the basic iterative

technique eliminates the high frequency components at different levels of coarsening. This leads to a rapid convergence to the final solution. The choice of prolongation and restriction operators in the multigrid setup is dependent on the nature of the grid used and the equation to be solved.

The discrete form of a pressure Poisson equation can be written as $AX = b$ where A is a sparse matrix, X is the vector of unknowns and b is the source vector. Depending on the Reynolds number the number of unknowns in the linear system could vary from a few millions to a few billions (limited by available memory and time on the computer). An efficient linear algebra solver is required to get results in reasonable time. There are several open source linear algebra packages like PETSc, HYPRE, Trilinos etc. But to choose an optimal set of solver and preconditioner for a given linear system is not an easy task. For the simulations presented here from the HYPRE package (Falgout *et al.* (2006)), a semi-coarsening based multigrid preconditioner (SMG) in association with GMRes (GMRES) as the solver, is used to solve the linear system.

2.10 Code Parallelization

DNS of the incompressible Navier-Stokes equations is computationally intensive with respect to both CPU time and memory (RAM) requirement. Most of the computational time is spent in the solution to the pressure Poisson equation. Low resolution(around 10^6 grid points) simulations can be run on a single processor but as the resolution increases the simulation has to be run on multiple processors. The solver was parallelized using 3D domain decomposition methodology, and MPI (Message Passing Interface) protocol was used for communication among processors. An equal number of processors was assigned to each direction. So, the total number of processors used was equal to N^3 where N represents the number of processors in each direction.

Chapter 3
Validation

Any numerical code developed to solve a physical problem has to be validated against benchmark experimental or numerical results in order to establish the accuracy and capability of the code. The validation exercise should involve standard benchmark cases and should also include cases relevant to the particular study. Our objective here is to study the evolution of a transient cumulus cloud flow. To the best of our knowledge no quantitative experimental or computational results are yet available for this case. In this chapter we therefore present comparisons between the results generated from our code and known results for related problems.

3.1 Lid-Driven Cavity Flow

Lid-driven cavity flow (2D and 3D) is a standard problem and has been studied extensively through CFD and laboratory experiments. The simplicity of the geometry and the unambiguous boundary conditions make the problem a standard benchmark for new computational techniques. With increasing Reynolds number the flow inside a cavity exhibits most of the phenomena observed in incompressible flows. A detailed review on this class of flows is given by Deshpande & Shankar (1994). We present the results for both 2D and 3D lid-diven cavity flows. Though 2D cavity flows are not physical, their computation has been studied extensively by solving the 2D Navier-Stokes equations.

For the 2D ($x-y$ plane) case, a cavity of aspect ratio 1 (square cavity) is considered here. The top lid at $y = 1$ moves with a tangential velocity of unit magnitude and zero normal velocity. The other walls have no penetration and no slip as the velocity boundary conditions. The simulations presented here are for a Reynolds number of 1000, and the results are compared with the results from Erturk (2009). Simulations are conducted for two different grid sizes, 128^2 and 256^2. The variation of horizontal (u) and vertical (v) velocities along the vertical (y) and horizontal (x) centerlines is shown in Figures 3.1 and 3.2 respectively. There is good agreement between present simulations and the benchmark test case. The results from the 256^2 grid simulation plot on top of those from the 128^2 grid simulation, which demonstrates the grid independence of the results.

For the 3D case, a cavity with square cross section and a spanwise aspect ratio (SAR)

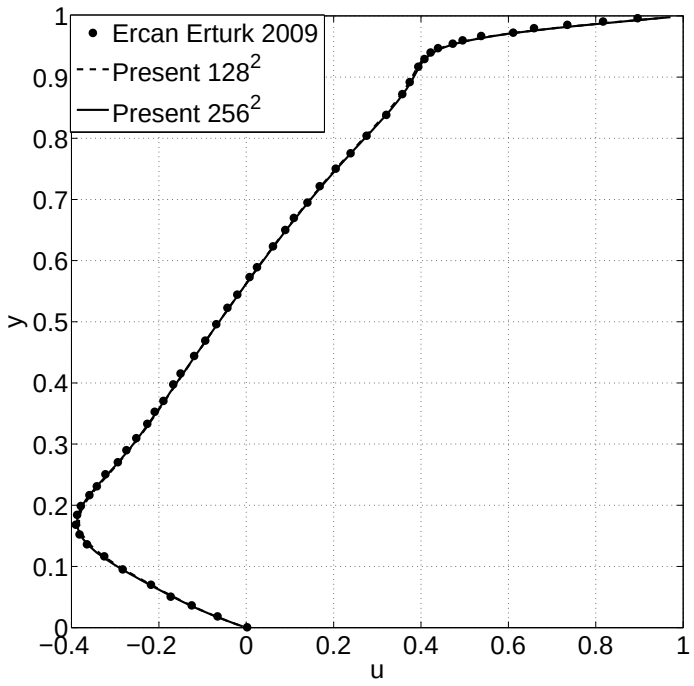

Figure 3.1: 2D Lid Driven Cavity. Variation of x velocity in the y direction at a Reynolds number of 1000.

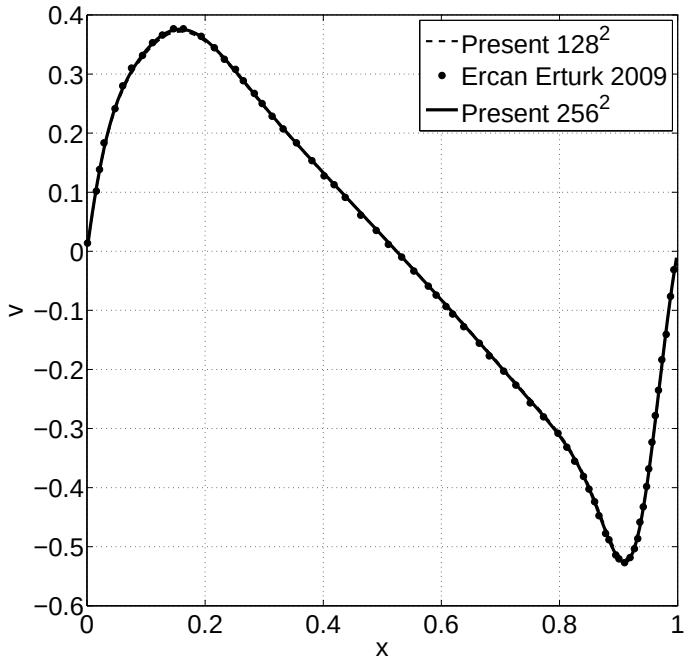

Figure 3.2: 2D Lid Driven Cavity. Variation of y velocity in the x direction at a Reynolds number of 1000.

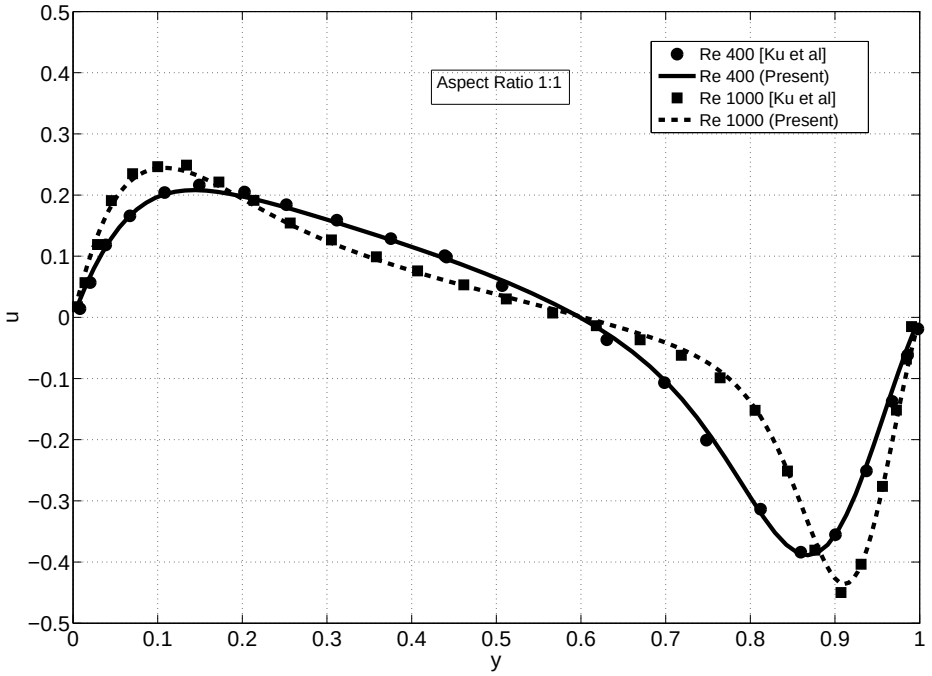

Figure 3.3: 3D Lid Driven Cavity. Variation of x velocity in the y direction on the symmetry plane at two different Reynolds numbers.

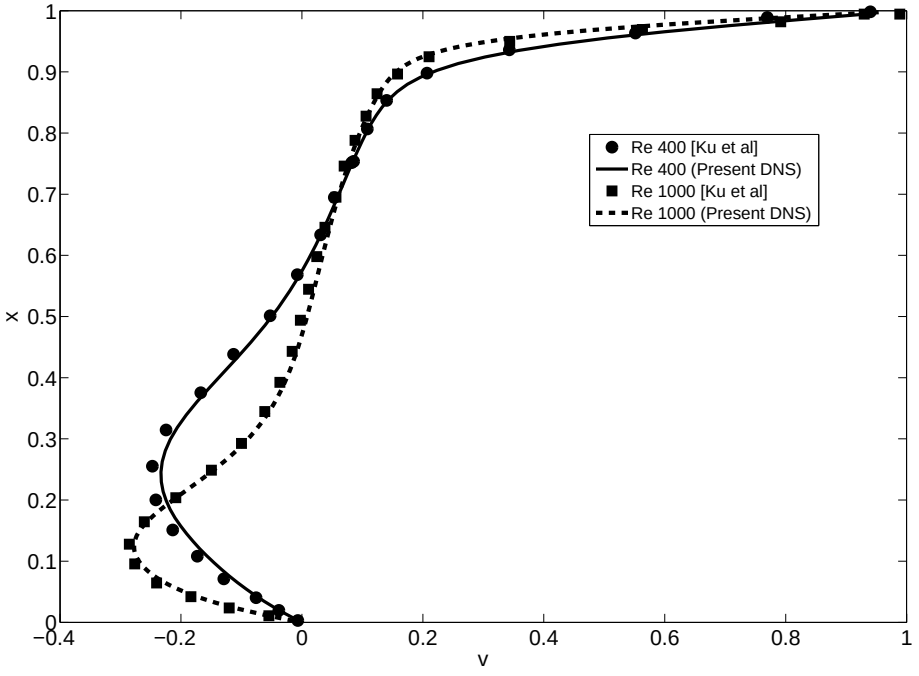

Figure 3.4: 3D Lid Driven Cavity. Variation of y velocity in the x direction on the symmetry plane at two different Reynolds numbers.

of 1 is considered here. The wall at $x = 1$ is given a tangential velocity of unit magnitude in the y direction and zero normal velocity. The other five walls have no slip and zero normal velocity as the boundary conditions. The results on the symmetry plane ($z = 0.5$) are discussed here. Calculations are performed for Reynolds numbers of 400 and 1000 on 64^3 and 128^3 grids respectively. The mesh is non-uniform in the x and y directions and uniform in the spanwise direction. The variation in x and y velocities on the symmetry plane, along the vertical and horizontal centrelines respectively, are shown in figures 3.3 and 3.4. The results from our computations agree with the pseudo-spectral calculations by Ku *et al.* (1987). It can be observed that the results from the 3D computations are different from those of the 2D computations at the same Reynolds number; the presence of walls in the spanwise direction has clearly altered the structure and the topology of the flow.

3.2 Laminar Rayleigh-Benard Convection

Rayleigh-Benard convection is a classical benchmark case for flows involving buoyancy effects and has applications in the area of atmospheric sciences. The non-dimensional parameters governing this flow are Rayleigh Number ($Ra = Re^2 Pr$) and Prandtl number (Pr). Extensive stability analyses of this flow have been performed to study the onset of convection. For benchmarking the code, this system is studied with air as the working medium (Pr = 0.71) and periodic boundary conditions are imposed in the horizontal directions for temperature, pressure and all velocity components. For this case the critical Rayleigh number is 1708. We present steady state results for a Rayleigh number of 4000. The bottom wall is maintained at a constant temperature T_h and the top wall is maintained at a lower constant temperature T_c. The governing equations are non-dimensionalised using $T_h - T_c$ as the temperature scale and the distance h between the top and the bottom plates as the length scale. Solid wall boundary conditions are imposed on the top and bottom walls. The dimensions of the domain in the periodic directions are $2.8h$. The acceleration due to gravity acts in the negative x direction. Solutions are computed using two different grids of size 16^3 and 32^3. The results reported here are from the larger grid. The system is initialised with a diffusion profile for temperature. Random fluctuations with zero mean and a maximum amplitude of 10 % of the temperature scale are superimposed on the base state temperature profile to trigger convection.

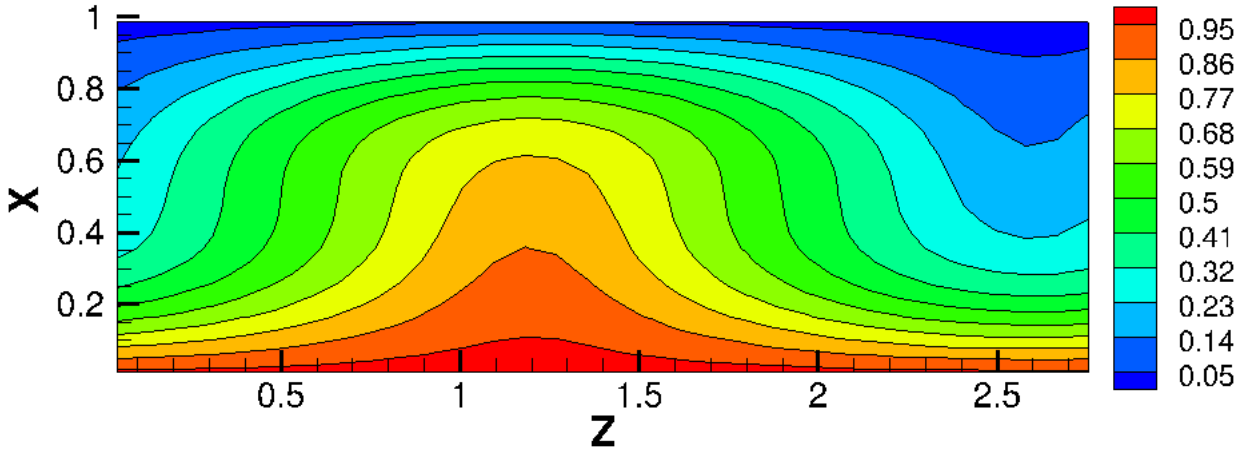

Figure 3.5: Non dimensional temperature contours on a vertical section at Ra = 4000.

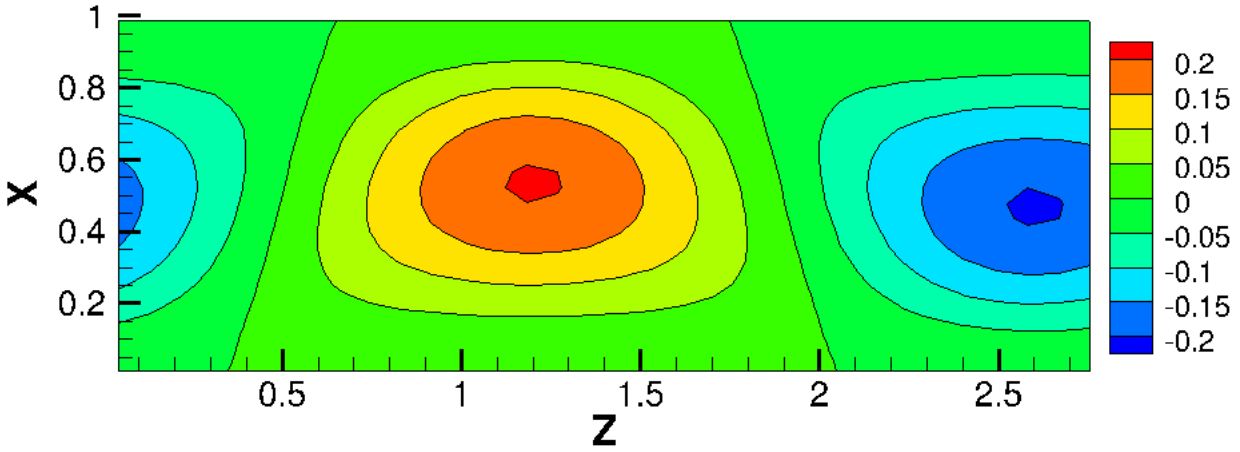

Figure 3.6: Vertical velocity contours on a vertical section at Ra = 4000.

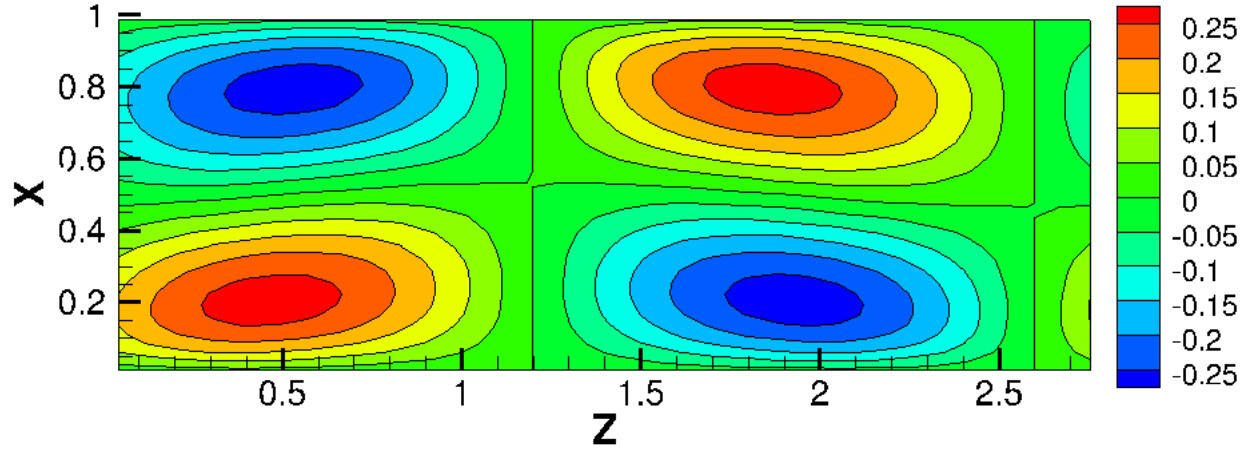

Figure 3.7: z velocity contours on a vertical section at Ra = 4000.

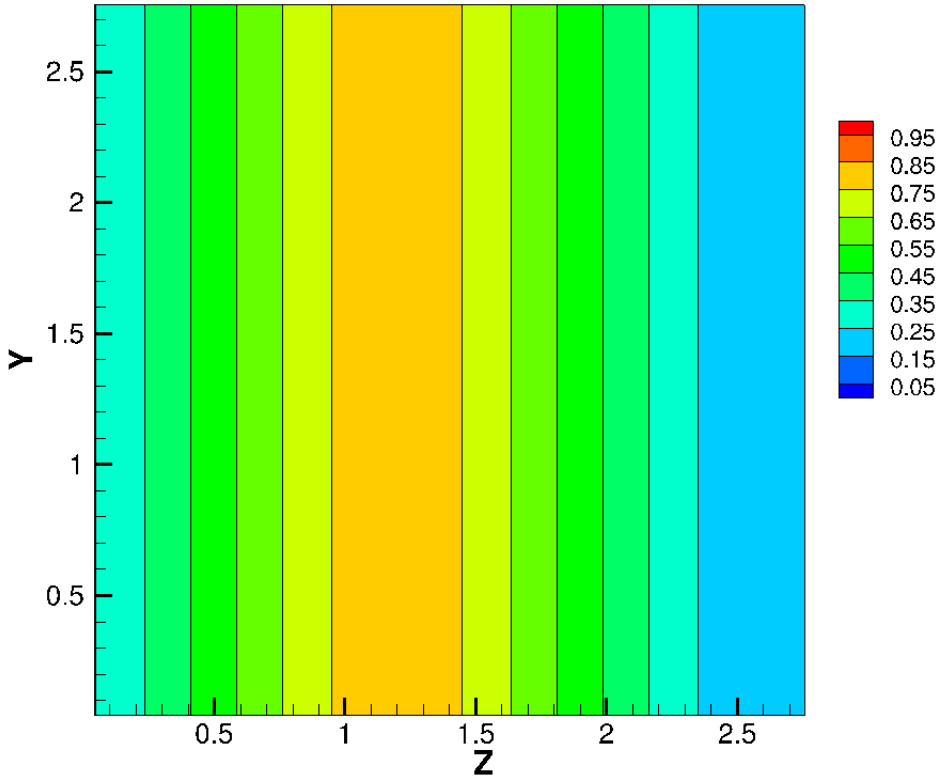

Figure 3.8: Temperature contours on a horizontal section at Ra = 4000. The flow field is two dimensional as the temperature field does not vary in the y direction.

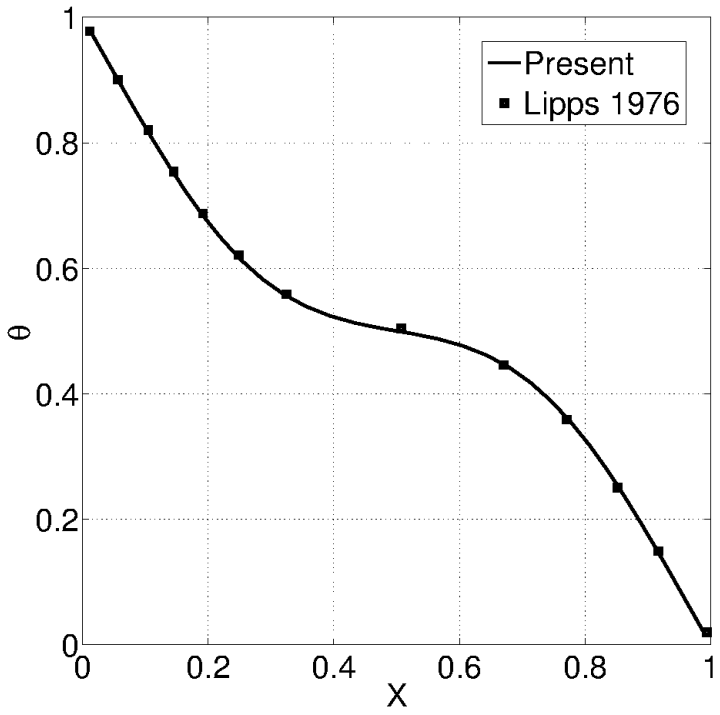

Figure 3.9: Variation of horizontal averaged non dimensional temperature in the vertical direction.

The qualitative features of the steady state flow field along a vertical section are given in figures 3.5 - 3.7. The temperature field (figure 3.5) depicts rising and descending plumes. A related horizontal section given in figure 3.8 shows that the flow is essentially two-dimensional. The observations reported here are consistent with the previously reported numerical results (Biringen & Peltier (1990), Lipps (1976)). Quantitative comparisons for average temperature variation are shown in figure 3.9. The averaging is done over space on a horizontal plane containing the two periodic directions. The distribution of average temperature between the two plates agrees well with the computations reported by Lipps (1976). The wall Nusselt number calculated from the present simulation is 1.7745, to be compared with those reported by Lipps (1976) 1.75 and Biringen & Peltier (1990) 1.79.

3.3 Turbulent Round Jet

A turbulent jet is an example of a free shear flow which has been studied through laboratory experiments and DNS. Jets play a significant role in propulsion, combustion, acoustics and mixing. Validating the solver with a free shear flow is relavant here because we intend to study the dynamics of a cumulus cloud flow, which again is a free shear flow. A particular problem with free shear flows is the specification of the appropriate boundary conditions to capture the entrainment accurately. Several laboratory experiments have been conducted to study round jets and two of them are considered as benchmark cases (Panchapakesan & Lumley (1993) - Reynolds Number $\sim 10^4$; and Hussein *et al.* (1994) - Reynolds Number $\sim 10^5$). These will be used to compare the results of our DNS simulations. DNS on a round jet has been performed at a Reynolds Number of 2400 by Boersma *et al.* (1998) and Babu & Mahesh (2004). They use different lateral and outflow boundary conditions but the converged statistics are in reasonable agreement with the experiments.

In the present study, simulations are conducted at a Reynolds number of 2400 based on exit velocity and exit nozzle diameter. Simulations were performed at two different grid sizes. Simulation A has a grid size of 10 million (200 x 200 x 250, x, y, z respectively), and simulation B has a grid size of ∼19 million (240 x 240 x 330). The details about the domain size and time step size for each simulation are given in table 3.1. A non-uniform grid similar to that in figure 2.3 is used to resolve the core flow better. The lateral boundaries are treated as walls and the bottom boundary is a wall with an orifice of diameter d through which flow enters the domain with a constant axial velocity of magnitude U_o (top hat profile). All flow variables are non-dimensionalised with U_o and d as scales. At the top (outflow) boundary, zero normal derivative condition is used for all the flow variables except pressure. For the pressure boundary condition the details are given in section 2.8.

Five diameters away from the outflow boundary the viscosity is increased by a factor of 20 to diffuse the vortical structures before interacting with the outflow boundary. It has been observed that with the existing outflow boundary conditions numerical instabilities originating from the outflow boundary propagate upstream in the absence of viscous padding.

Simulation	Domain-Size (x,y,z)	Grid-size	Timestep-size
A	(100,100,50)	(240,240,330)	0.005
B	(100,100,45)	(200,200,250)	0.005

Table 3.1: Simulation details

The inflow field is perturbed by adding pseudo-random noise with zero mean and uniformly distributed with an amplitude of 0.1 % of U_o on to the top hat profile at each time step. An initial stage of upto $t = 1250$ was computed to allow all transients to leave the domain. Statistics were calculated over $1250 < t < 2500$ for simulation A and $1250 < t < 3000$ for simulation B. The computations were performed in the ICE cluster (SGI Altix ICE 8400 EX cluster, Intel Xeon CPU X5670 2.93 GHz dual six-core processor nodes w/Infiniband) at CSIR - 4PI, Bangalore. The statistics and other quantities calculated from the simulations are discussed below.

In figure 3.10 the variation of the inverse of the center line velocity with axial distance is plotted. The solid line represents the result from the present DNS and the broken line represents a linear fit of the form

$$\frac{1}{U_c} = \frac{1}{B_u}[z - z_o] \tag{3.1}$$

to the data points in the range $22 < z < 37$. The parameters obtained from the curve fit are compared with three other results. The summary is given in table 3.2.

Quantity	Panchapakesan & Lumley (1993)	Hussein *et al.* (1994)	Boersma *et al.* (1998)	Present (Sim. A)
Reynolds number	$\approx 10^4$	$\approx 10^5$	2.4 x 10^3	2.4 x 10^3
B_u	6.1	5.8	5.9	6.2
z_o	-	4.0	4.9	5.45

Table 3.2: Parameters obtained from the linear fit for the decay of the mean centerline velocity with axial distance.

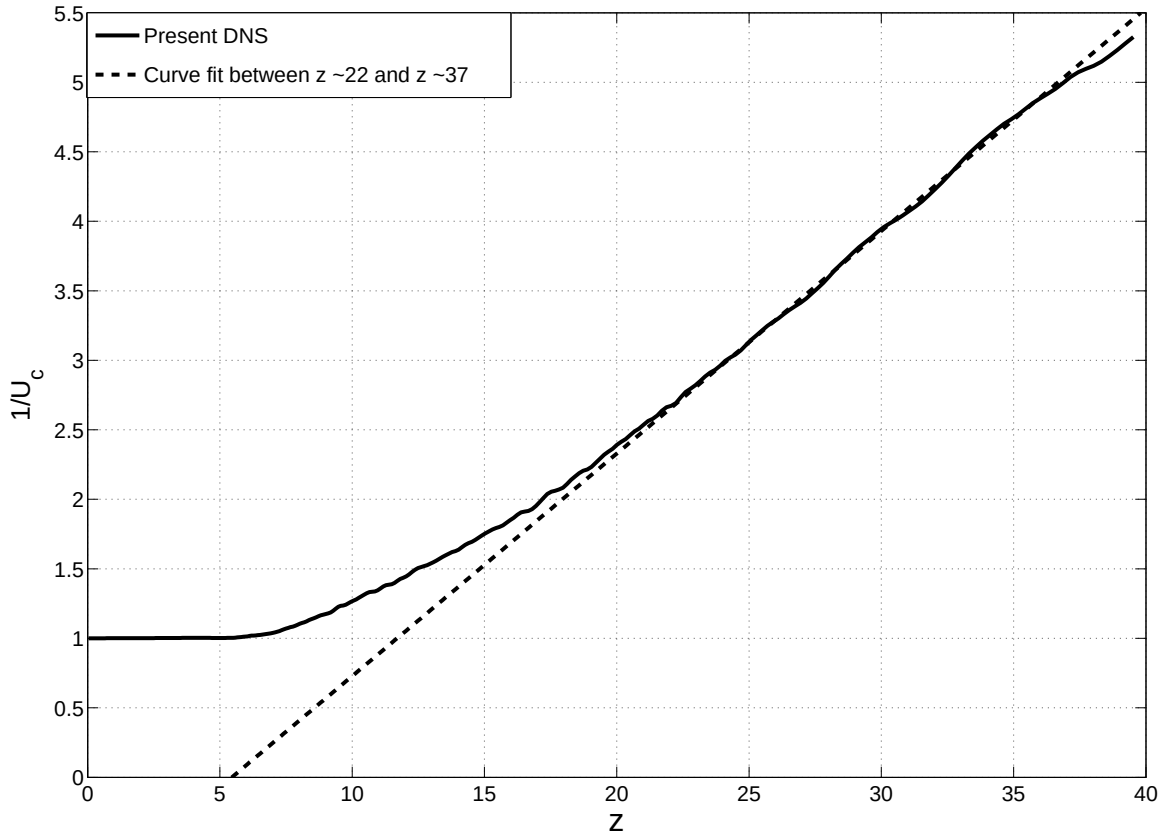

Figure 3.10: The inverse of the centerline velocity non dimensionalised with the inlet velocity plotted against the axial distance from the inlet. The curve fit is obtained from the equation 3.1.

The inverse dependence of the centere line velocity on the axial distance is evident from the plot in figure 3.10. The parameter z_o, known as the virtual origin, and the constant B_u are functions of experimental conditions and the noise introduced at the inflow. So these two parameters may vary from case to case. The value of B_u reported here is close to the values reported by Panchapakesan & Lumley (1993) and Hussein *et al.* (1994).

The streamwise variation of the turbulence intensities in all the three directions, and the maximum Reynolds shear stress, are plotted in figure 3.11. It can be observed that the maximum Reynolds shear stress acheives an asymptotic limit around $z >= 25$. The axial intensity does the same at $z >= 30$ and the radial, azimuthal intensities appear to saturate around $z = 35$. These observations are consistent with experimental findings from which it is known that the Reynolds shear stress attains self similarity before the turbulence intensities. A similar observation has been reported in the DNS calculations of Boersma *et al.* (1998).

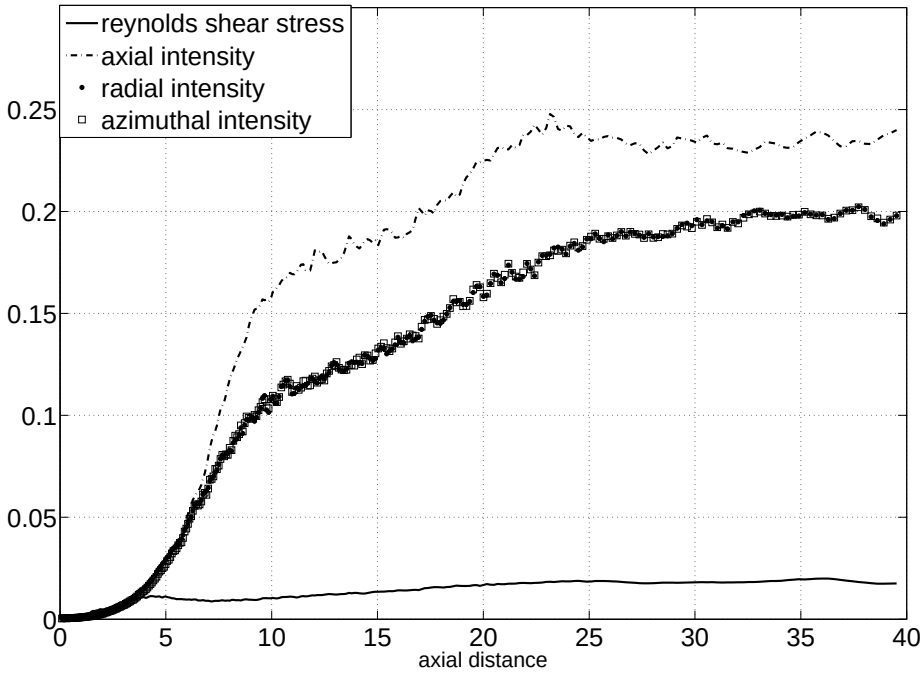

Figure 3.11: The variation of the normalised centerline turbulence intensities in all directions and the maximum of normalised Reynolds shear stress at a given height as a function of axial distance.

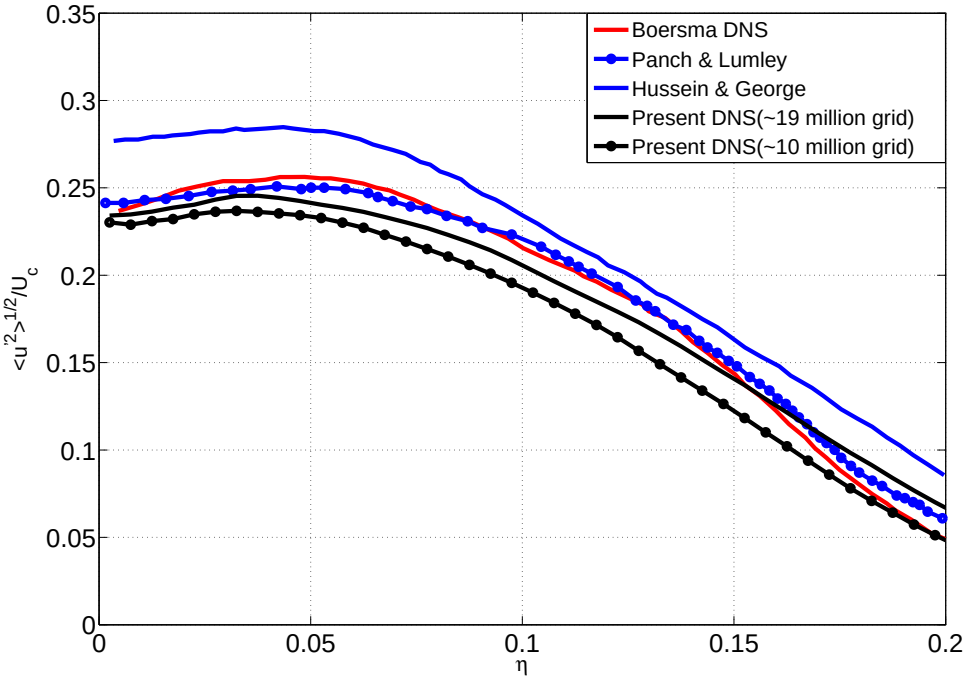

Figure 3.12: Turbulence intensity in the axial direction normalised with the local centerline velocity as a function of the similarity variable η. The legend explains the various cases plotted.

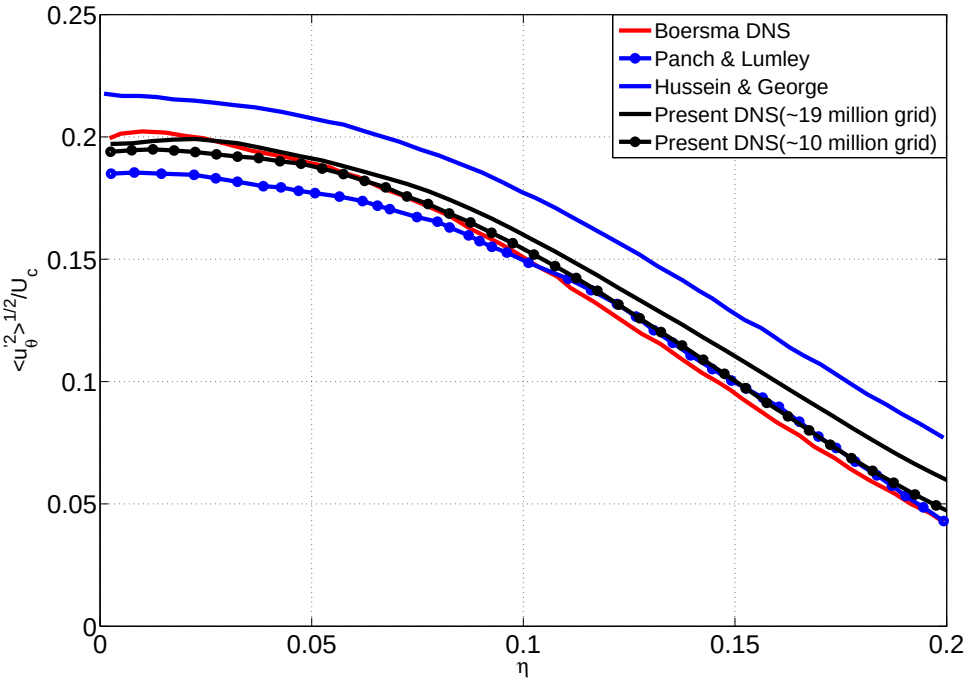

Figure 3.13: Turbulence intensity in the azimuthal direction normalised with the local centerline velocity as a function of the similarity variable η. The legend explains the different cases plotted.

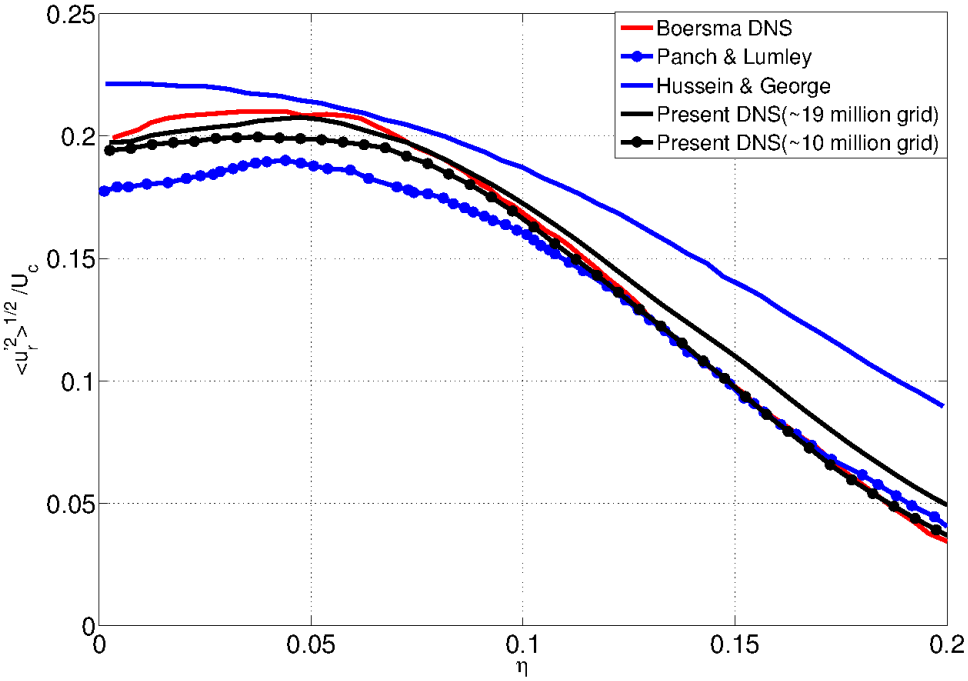

Figure 3.14: Turbulence intensity in the radial direction normalised with the local centerline velocity as a function of the similarity varaible η. The legend explains the various cases plotted.

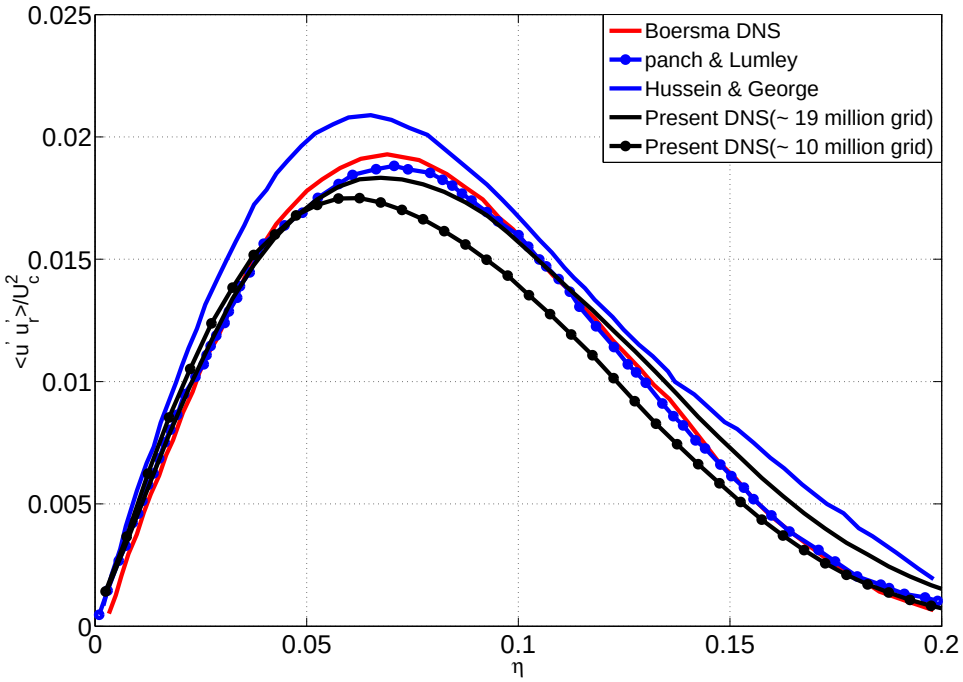

Figure 3.15: The Reynolds shear stress normalised with the local centerline velocity as a function of the similarity varaible η. The legend explains the various cases plotted.

In figure 3.12 we plot the variation of normalised axial turbulence intensity against the similarity variable $\eta = (r/(z - z_o))$. The axial intensity profiles are averaged over $32 < z < 40$. Figures 3.13 and 3.14 give the variation of normalised azimuthal and radial turbulence intensities against η. The profiles are averaged over $35 < z < 40$. Figure 3.15 plots the normalised Reynolds shear stress averaged over $28 < z < 38$ against the similarity variable. In these figures it can be seen that the solution improves as the grid resolution improves. The results obtained from the higher resolution simulation reproduce the trends observed in the laboratory experiments. There exist some differences between the present DNS results and the experiments. First of all the two experiments used as the benchmark cases here do not agree between themselves. There could be several reasons for these differences. The resolution in simulation A may not be sufficient to capture all the scales; from Babu & Mahesh (2004) it can be observed that with higher grid resolution the statistics improve. Another reason for the difference could be that in the DNS calculation the higher order quantities may not have reached a self-similar state due to the smaller domain sizes when compared to the laboratory experiments.

Chapter 4

Results and Discussion

We present here preliminary results from a series of exploratory simulations, whose main objective was to derive certain features of cloud flows in general.

4.1 Cloud flow configuration

The cumulus flow is here modelled as a transient diabatic plume (section 1.2). The governing equations are discussed in section 2.2. The flow schematic for the cloud flow is given in figure 4.1. Several geometrical parameters are involved in this configuration. The region between z_b and z_t represent the heat injection zone (HIZ). Off-source buoyancy is added to the flow inside the HIZ. The horizontal extent of the HIZ is determined by tracking the edge of the flow using a passive scalar field. The heat injected within the HIZ varies both in space and time. The boundary conditions for the simulations are discussed in section 2.8. The simulations are carried out at a Reynolds number of 2000 and a Prandtl number of 1.0. The details about the domain size and time-step are given in table 4.1.

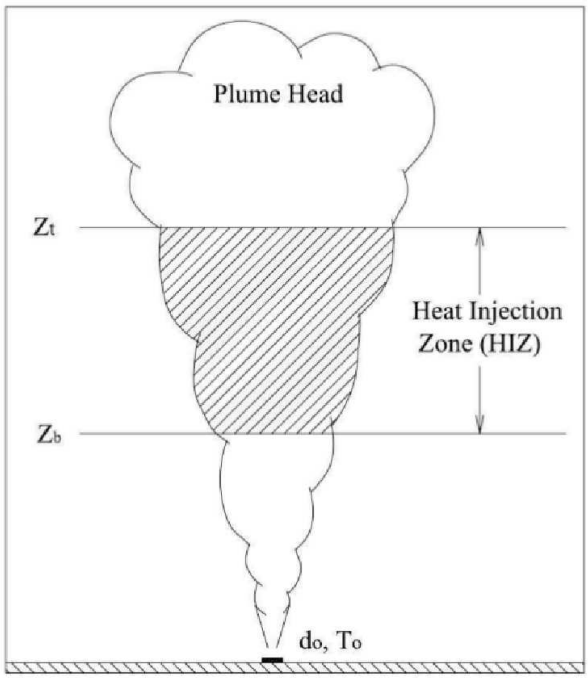

Figure 4.1: Flow schematic. (Ref Konduri (2009))

Simulation	Domain-Size (x, y, z)	Grid-size	Timestep
A	(40,40,40)	(128,128,256)	0.005
B	(70,70,39.9)	(402,402,798)	0.0025

Table 4.1: Simulation details

Several exploratory runs were carried out to check the capability of the solver to simulate cloud flows. These runs were carried out using the coarse grid A (Table 4.1). Temperature noise with zero mean and an amplitude of 10% is added to the warm source patch at $z = 0$ to trip the flow. Figure 4.2 shows two pairs of natural clouds and the present numerically computed clouds. The computed flow field is represented as a cloud by suitably thresholding the passive scalar concentration to define the cloud edge, and was volumetrically rendered using PARAVIEW (ParaView (2008)). While comparing the two images it should be remembered that cumulus clouds are turbulent free shear flows and no two images of a cloud, whether in nature or in computation, will ever be identical. So the comparison should be based on the broad features based on the attributes described in WMO (1975). Figure 4.2 depicts two types of cumulus clouds - one that rises up like a tower (figure 4.2a) and one with a cauliflower shaped head (figure 4.2b). The present numerical simulations (simulation A) represent these two clouds qualitatively.

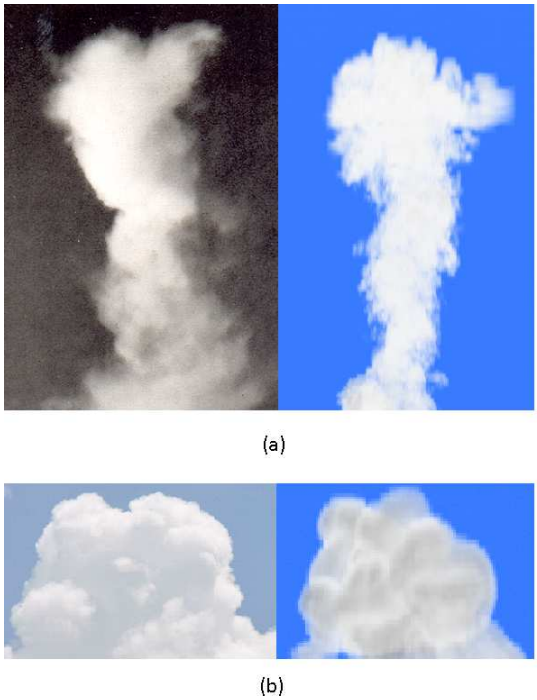

Figure 4.2: Comparison of real cloud (left) and numerical simulation (right)

4.2 Gallery of Cloud Flows

In this section we illustrate the role played by heating profiles, and show how variations in heating history can significantly affect the evolution of the flow. Simulations were carried out using the coarse grid resolution A. At $t = 0$, all the flow variables are set at zero, the temperature is switched on over the hot patch. The plume solution is integrated till the plume head enters the heat injection zone, which occurs at $t \approx 50$. The solution at this time is saved and is used as the initial condition to study the effect of different heating histories on the evolution of the flow. Not much information is available on the vertical extent of the HIZ and the horizontal variation of the heat release function in natural clouds. These parameters were therefore fixed based on trial runs numbering more than 15. Of all the simulations performed, a set of four distinct results are shown here. Two different HIZ heights and two different horizontal heat distribution functions have been tested in these simulations. The details are given in Table (4.2).

Simulation No.	**HIZ extent**	**Horizontal heat distribution**	**Heating profile**
1	10 - 12.5	gaussian	figure 4.11 a
2	10 - 12.5	bimodal	figure 4.11 a
3	10 - 12.5	gaussian	figure 4.11 b
4	10 - 15	gaussian	figure 4.11 c

Table 4.2: Index for the Gallery

In the visualisation images presented here only the region above the base of the HIZ (i.e $z >= z_b$) is shown. The evolution of the flow with different heating profiles at different time instants is shown in figures 4.3 - 4.10. At each instant two views, 90 degrees apart in the azimuthal direction, are shown. It can be observed that at a given instant the flow field is not axisymmetric. The variable t in each snapshot represents the time after the heat injection starts. Simulations 1 and 2 have the same heating profile along the axis and the same heating history in time. The only difference is in the horizontal distribution at each vertical zone. But the evolution of the cloud flow in the two cases is significantly different. The gaussian heat distribution with peak at the axis rises very rapidly and forms a bulbous head only at later stages, whereas the bimodal heat distribution forms the bulbous head fairly early. So the heat distribution in both space and time plays a significant role in determining the shape of the cloud flow.

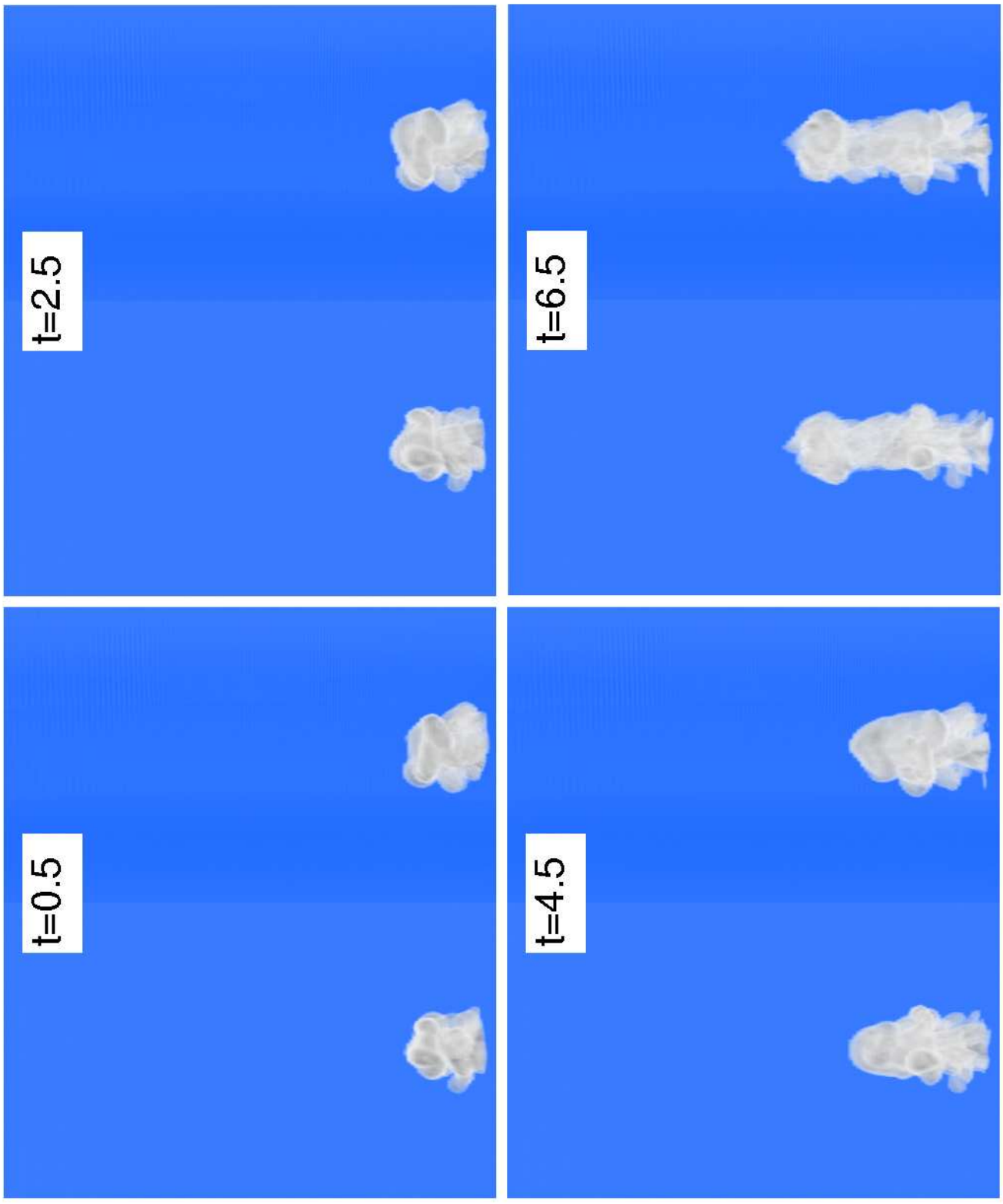

Figure 4.3: Simulation 1

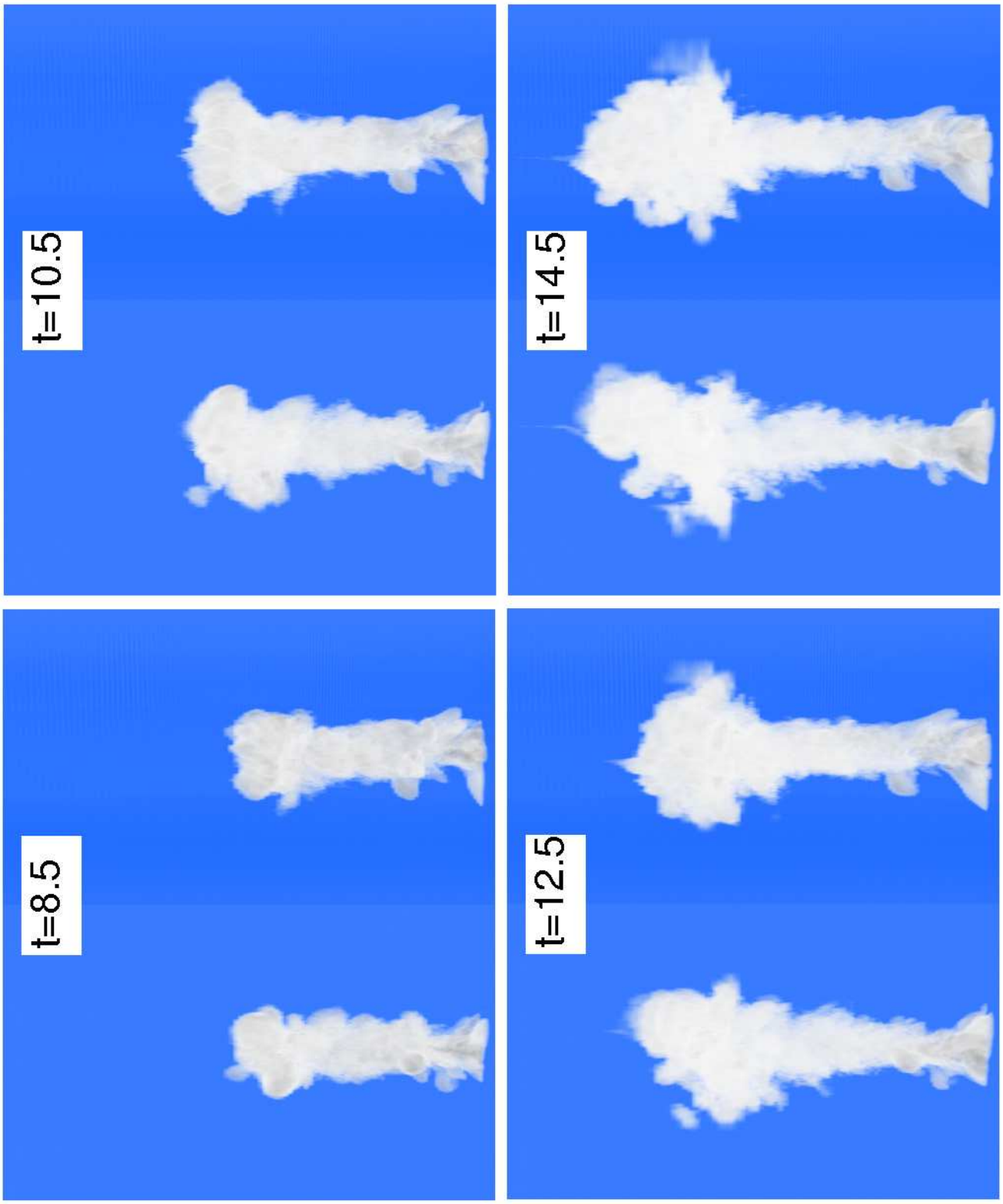

Figure 4.4: Simulation 1 continued

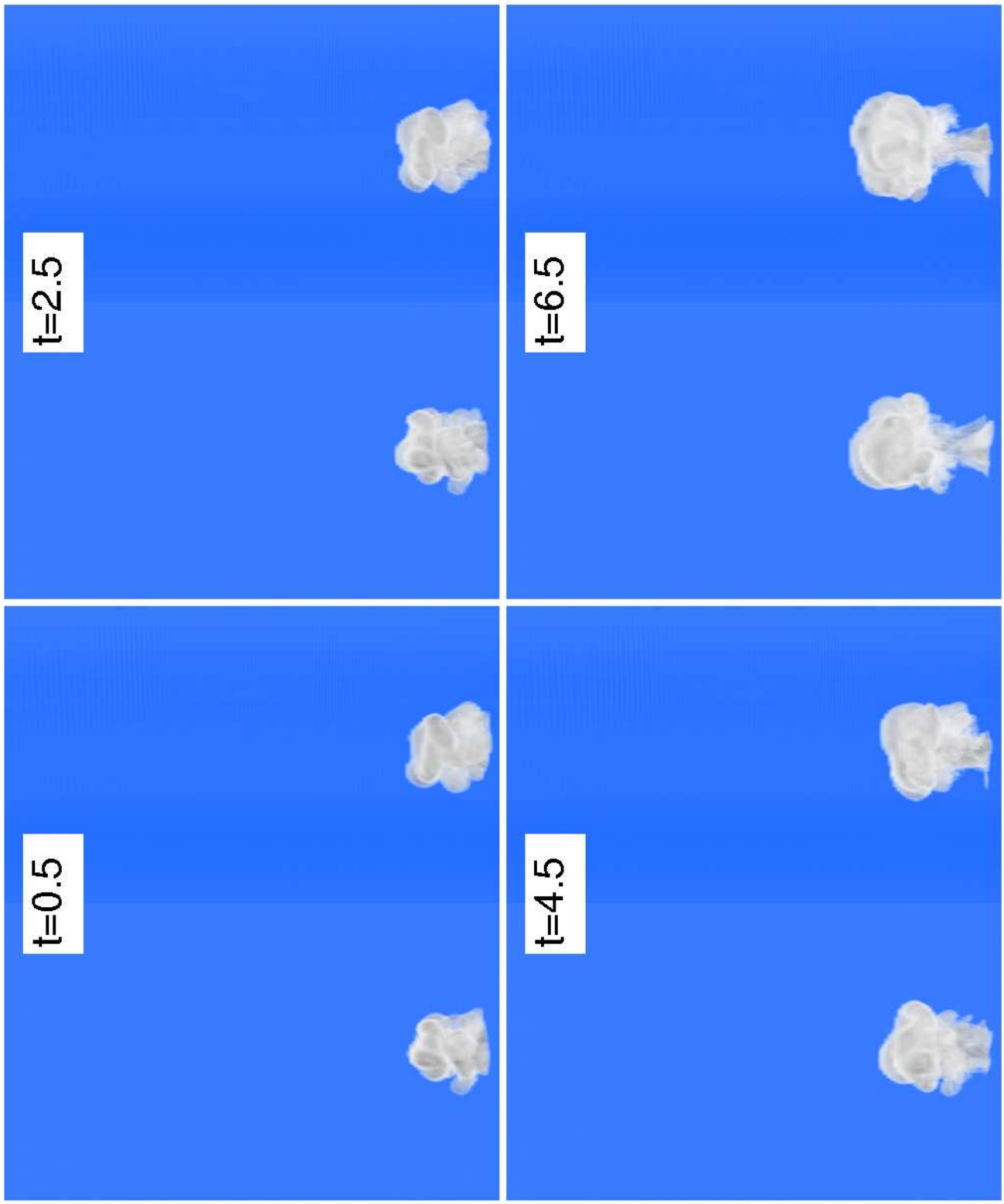

Figure 4.5: Simulation 2

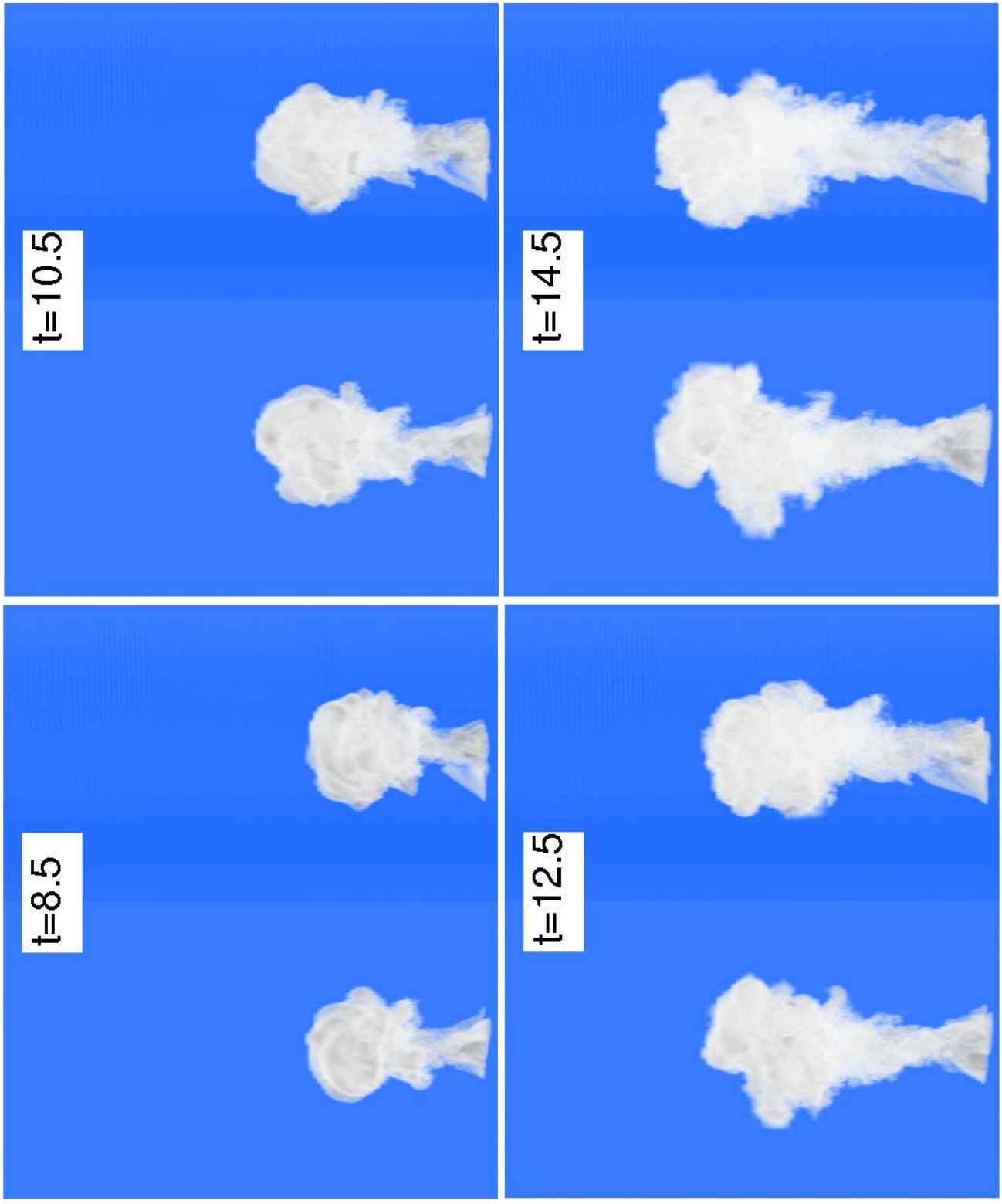

Figure 4.6: Simulation 2 continued

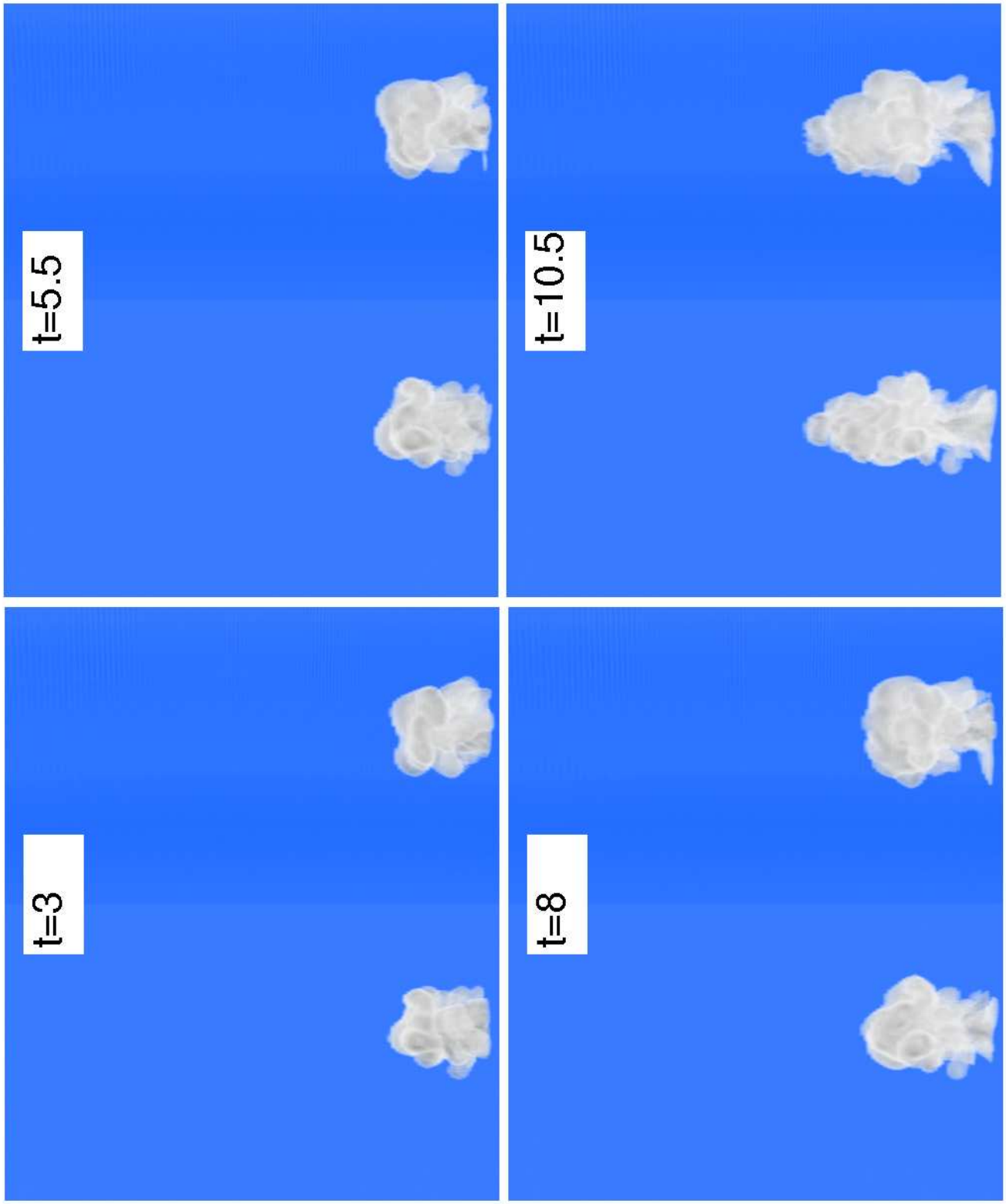

Figure 4.7: Simulation 3

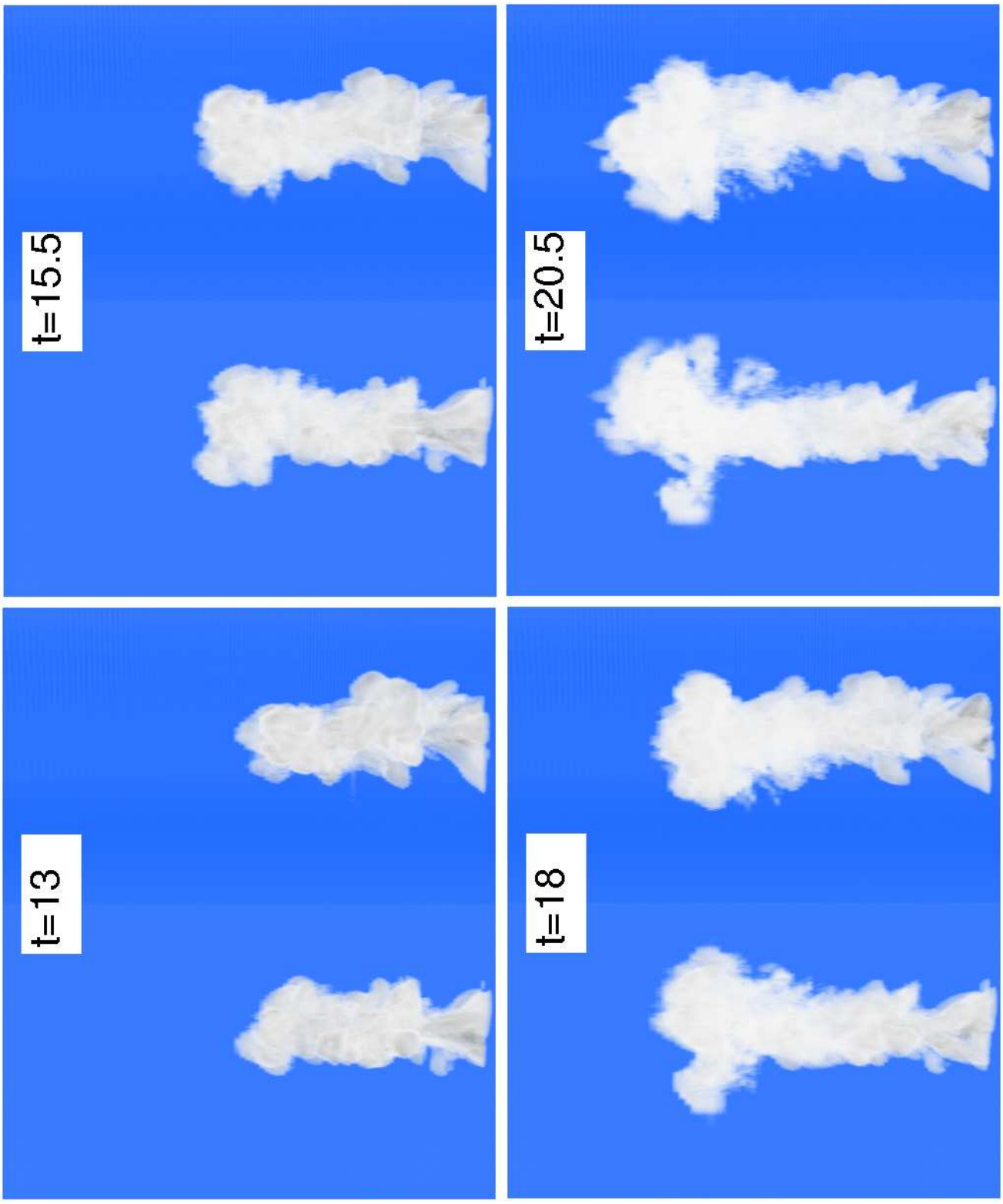

Figure 4.8: Simulation 3 continued

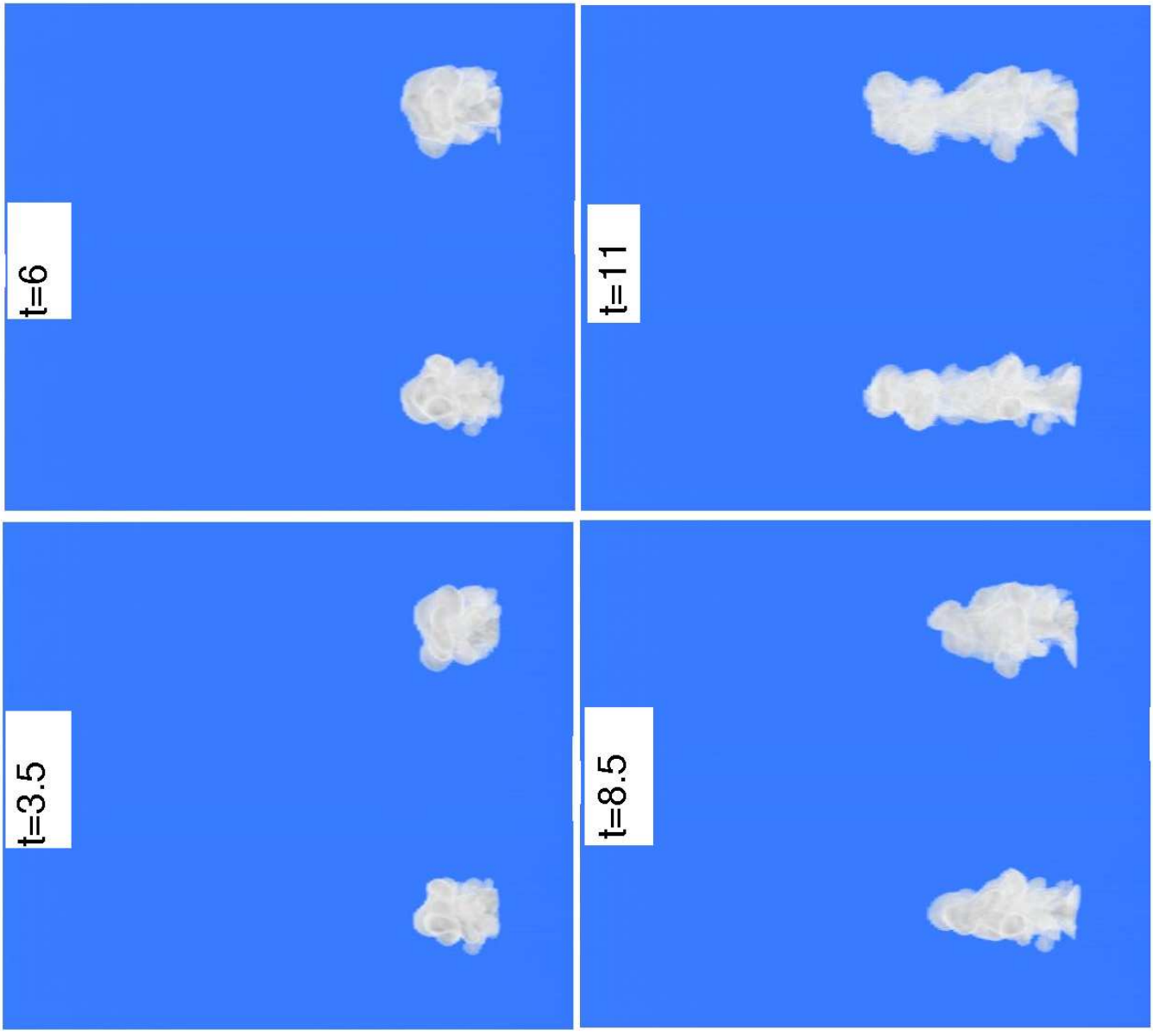

Figure 4.9: Simulation 4

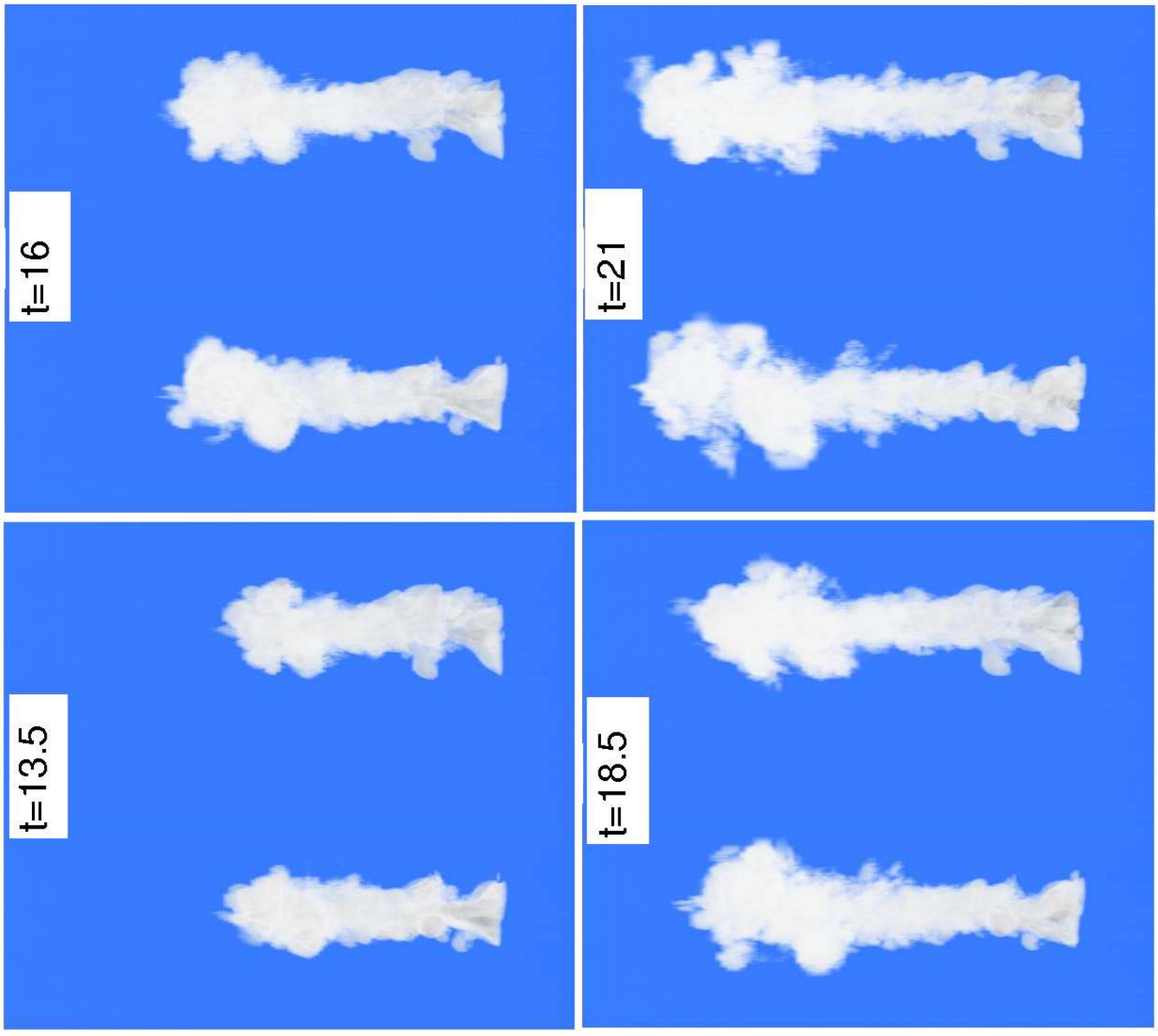

Figure 4.10: Simulation 4 continued

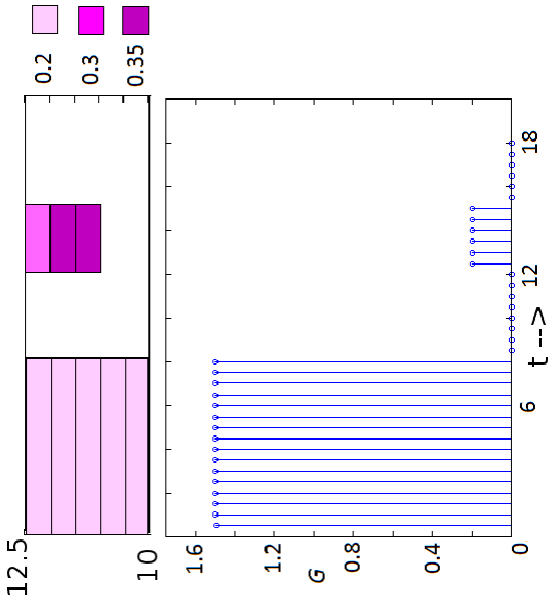

(a) Simulation 1 and 2

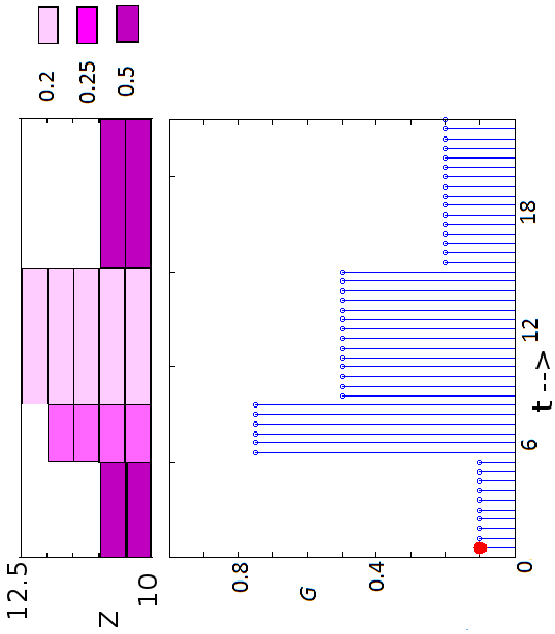

(b) Simulation 3

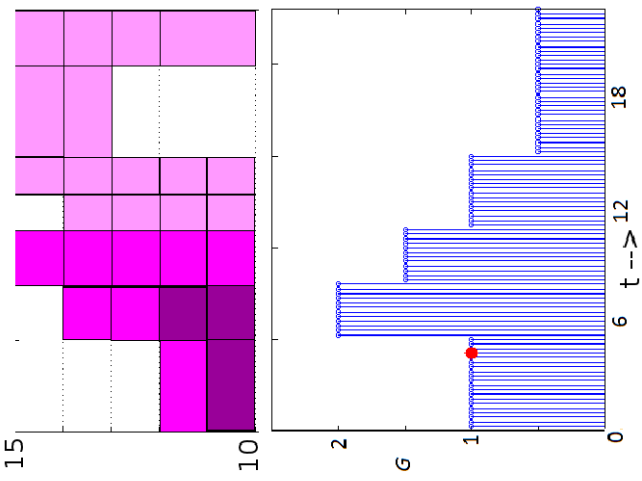

(c) Simulation 4

Figure 4.11: Heating Profile

4.3 Edge Detection: Cloud Flow

In a real cloud a distinct edge is defined by the presence of water droplets or ice particles. In the present numerical simulation several parameters, including the passive scalar concentration, temperature field, velocity thickness and vorticity magnitude have been used to detect the boundary of the active flow. We use the magnitude of the vorticity vector to define the edge separating the cloud flow from the ambient. Similar ideas have been used previously (Mathew & Basu (2002),Bisset *et al.* (2002)) to distinguish between the irrotational ambient fluid and turbulent rotational fluid. In figures 4.12a and 4.13a axial sections of the thresholded vorticity magnitude are shown at two different angles (90 degress apart) and in figures 4.12b and 4.13b the corresponding azimuthal vorticity field with the velocity vectors superposed are presented. It can be observed that the edge of the flow can be clearly represented as the magnitude of the vorticity vector varies sharply in the radial direction close to the edge of the flow, particularly near the head. The thin green layer in figures 4.12a and 4.13a appears to behave like the viscous super layer of Corrsin & Kistler (1955) separating the rotational and irrotational regions. In figures 4.12b and 4.13b the pink arrows represent positive axial velocity and the blue arrows represent negative axial velocity. This form of representation of the flow field gives clear information on the presence of ring like vortical structures close to the edge of the flow. For instance, the vortex on the top right is clearly visible; the structure is engulfing fluid from below and expelling fluid from the top. Other such less prominent structures are similarly visible on either side of the active flow.

4.4 Effect of off-source buoyancy

The most noticeable effect of off-source buoyancy addition is the reduction in the spreading rate of the evolving flow. From figures 4.12a and 4.13a it can be observed that the flow rises like a tower and does not spread like a classical plume or a jet. Figures 4.14 and 4.15 show a three-dimensional comparison of the vortical structures between an unheated transient plume and a diabatic transient plume. In the unheated case well-organised structures can be seen, as opposed to the diabatic case where beyond HIZ the structure of the flow undergoes a drastic change. The high frequency structure is richer in both aziumthal and axial vorticity. It can be observed that the large scale oraganised motion is disrupted/ruptured due to the injection of off-source buoyancy. Similar observations were reported by Basu & Narasimha (1999) in their temporal simulation of a cloud flow in a box. The disruption of large scale vortical structures may have a tremendous effect on the entrainment parameter.

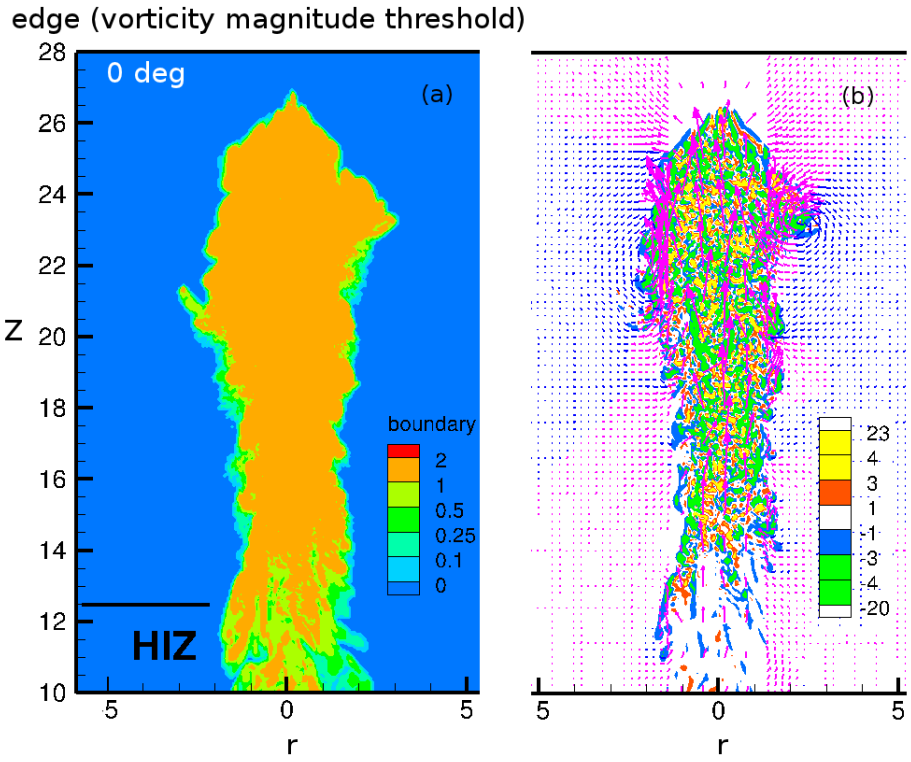

Figure 4.12: Axial section (at $\theta = 0$ deg.) of a diabatic plume: (a) Edge of the flow defined based on vorticity magnitude as threshold. (b) Azimuthal vocticity contours with velocity vectors superposed

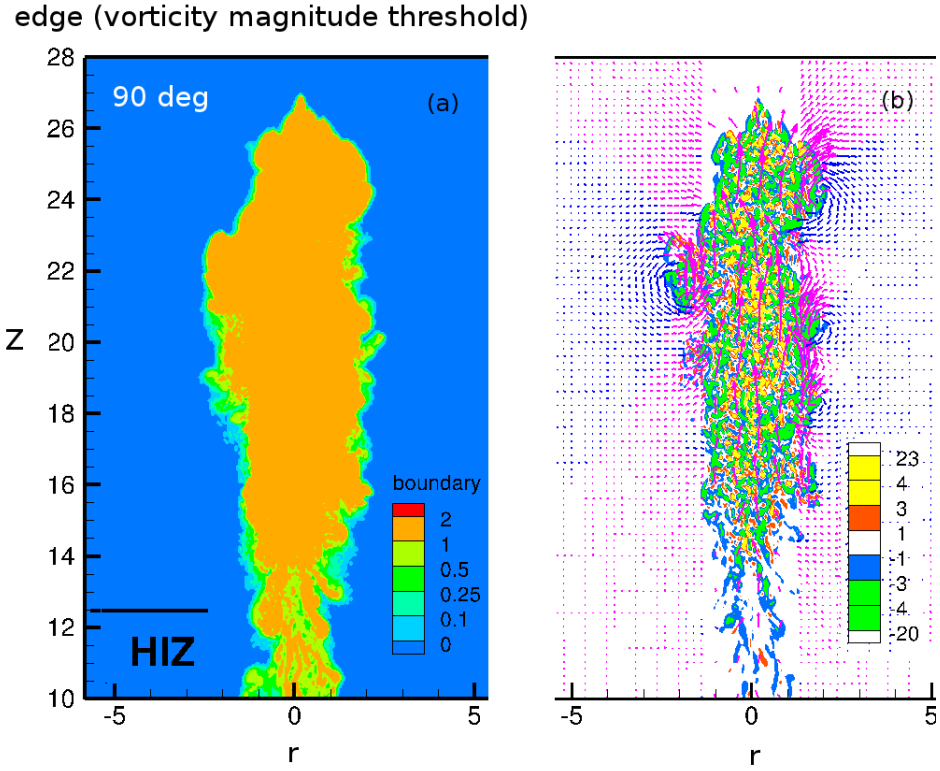

Figure 4.13: Axial section (at $\theta = 90$ deg.) of a diabatic plume: (a) Edge of the flow defined based on vorticity magnitude as threshold. (b) Azimuthal vocticity contours with velocity vectors superposed

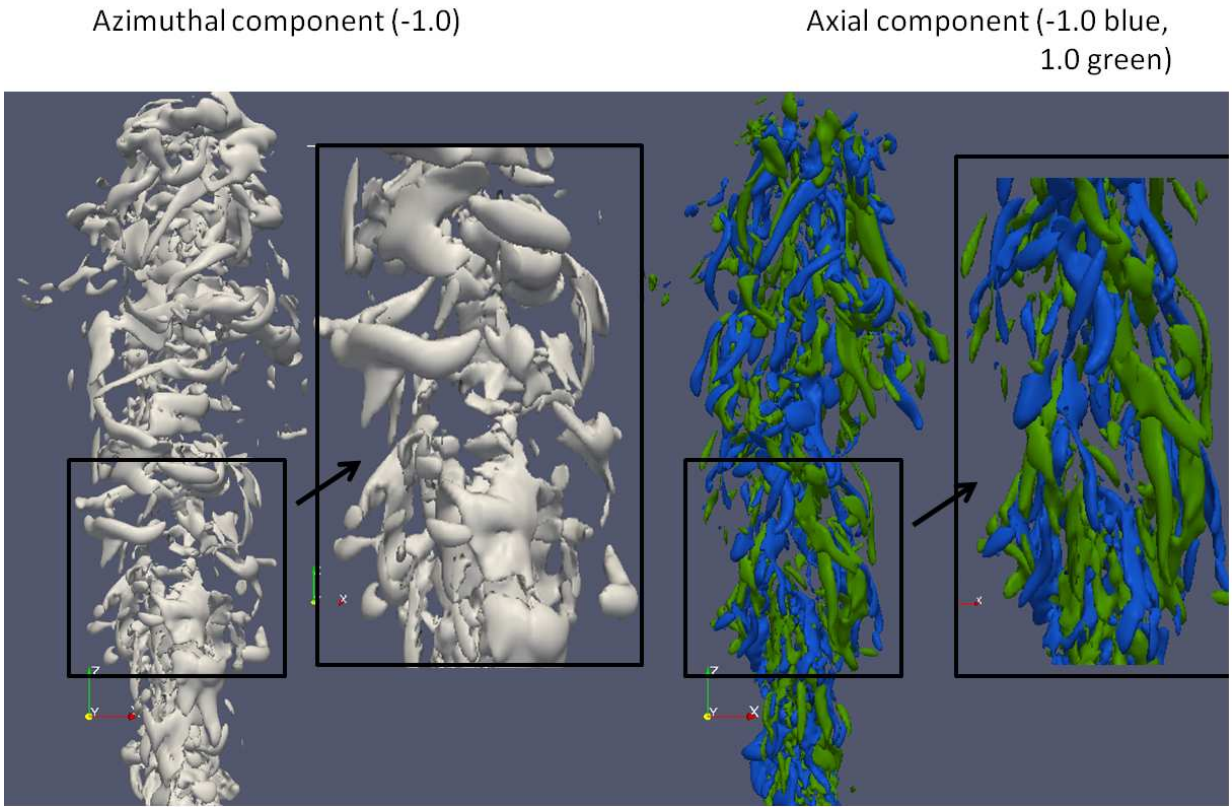

Figure 4.14: Non-diabatic plume: Vorticity iso-surface

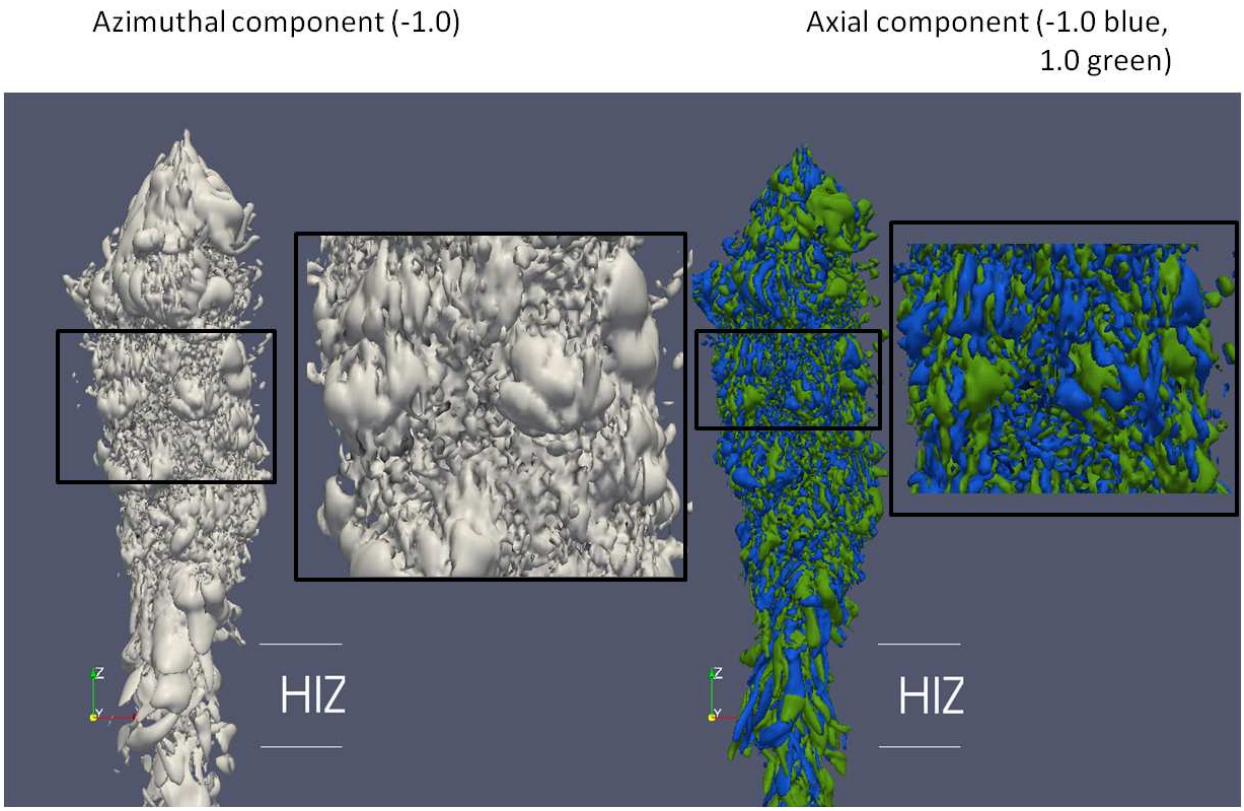

Figure 4.15: Diabatic plume with heat addition: Vorticity iso-surface

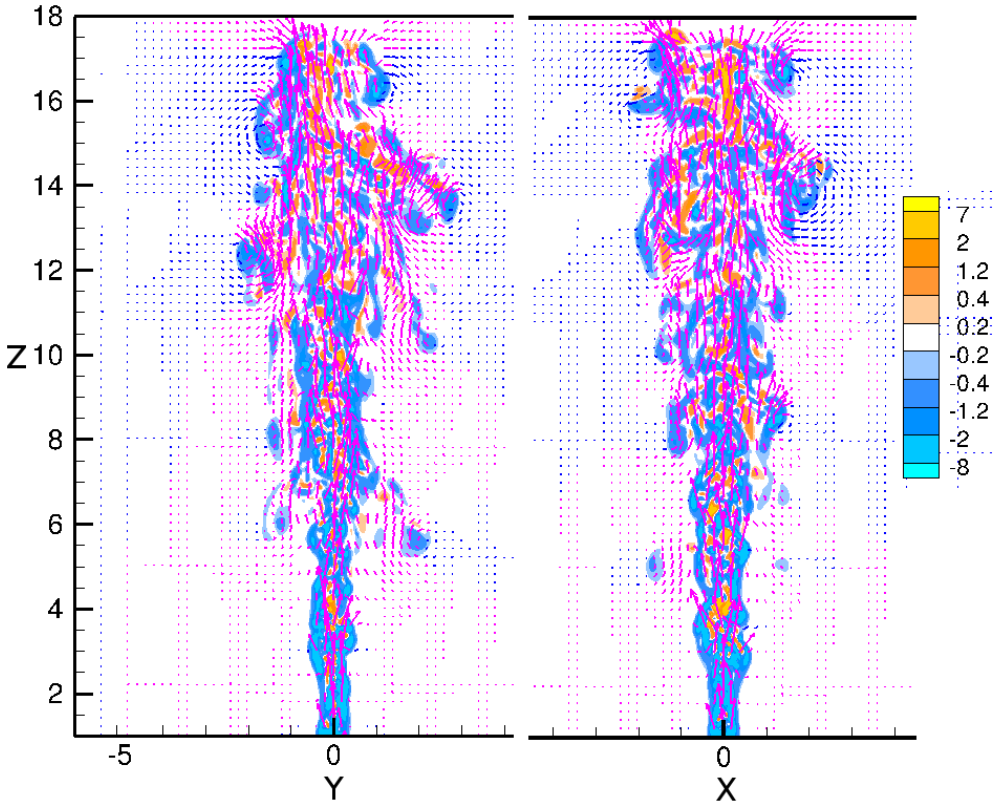

Figure 4.16: Axial section of non-diabatic plume at two different azimuth angles 90 deg. apart. The contours represent the azimuthal vorticity field and the vectors represent the velocity field. Pink arrows represent rising motion and blue arrows represent sinking flow

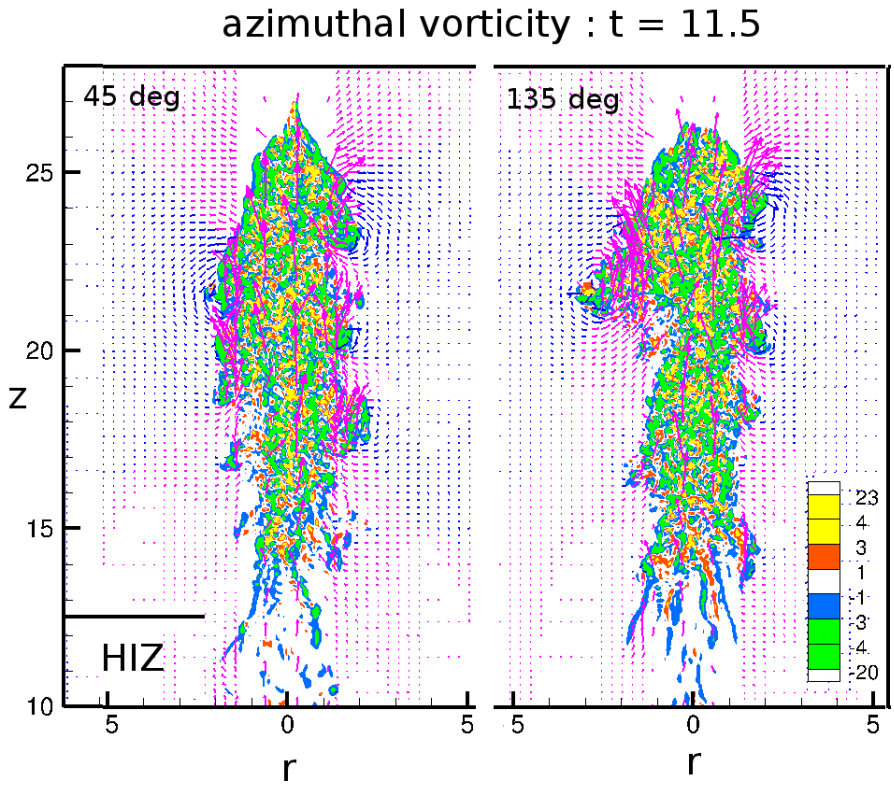

Figure 4.17: Axial section of diabatic plume above HIZ at two different azimuth angles 90 deg. apart. The contours represent the azimuthal vorticity field and the vectors represent the velocity field. Pink arrows represent rising motion and blue arrows represent sinking flow

Figures 4.16 and 4.17 show axial sections for a transient plume and a diabatic plume post heat injection, representing the azimuthal vorticity field superposed with velocity vectors (pink arrow for rising flow and blue arrow for sinking flow). It can be seen that the core of the diabatic plume is disorganised and the azimuthal vorticity is higher by an order of magnitude when compared with the unheated plume scenario. Azimuthal vorticity of both signs are present, but close to the edges the negative (shear enhancing) vorticity is dominant except close to the head. No large scale organisation is seen in the diabatic plume.

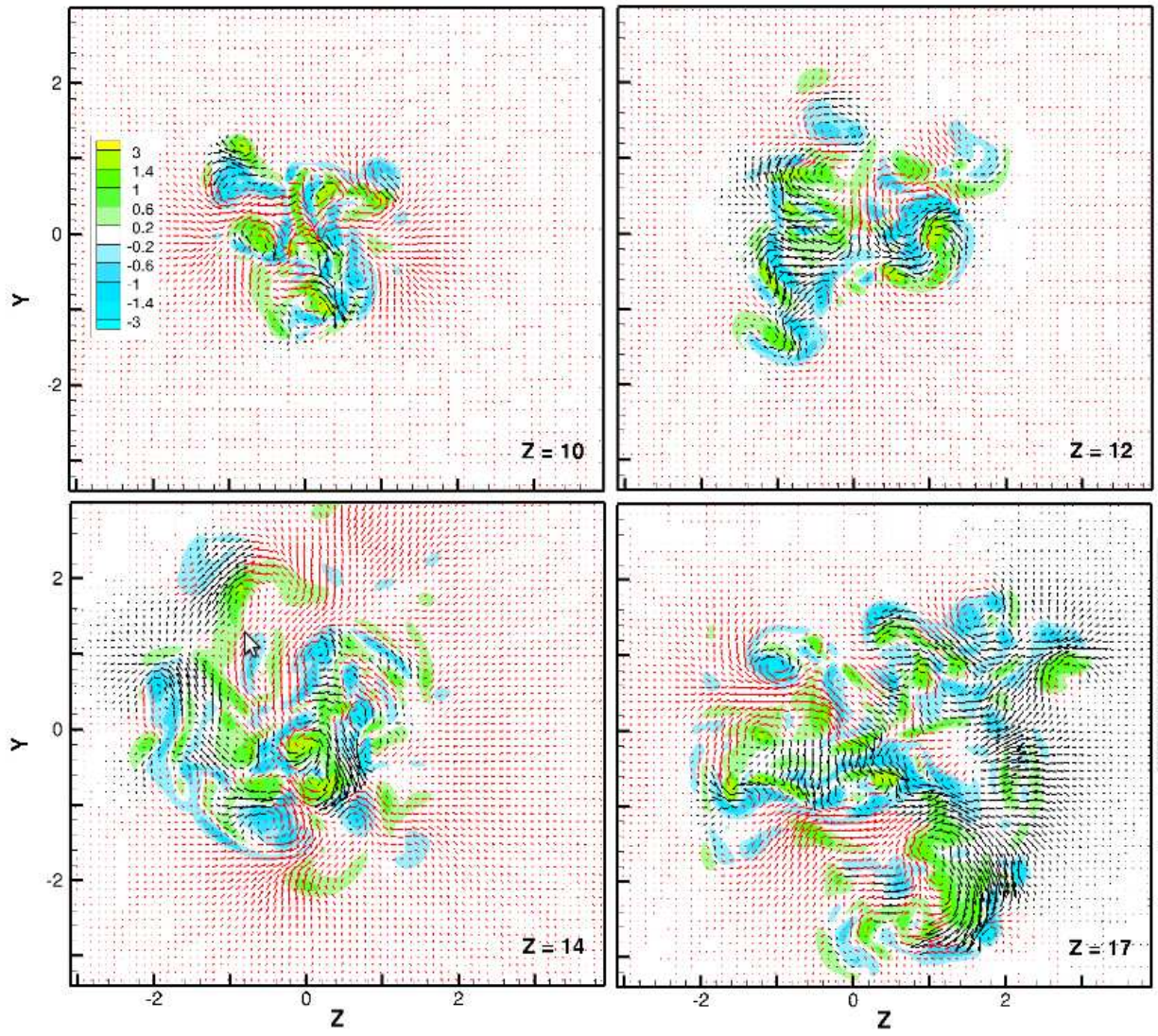

Figure 4.18: Diametral section of a non-diabatic plume at different axial distances. The contours represent axial vorticity field, inward velocity vectors are red and outward velocity vectors are black.

Figures 4.18 and 4.19 show diametral sections at various heights for transient plumes, non-diabatic and diabatic respectively; here the velocity vectors in the plane of the section are superposed on the axial vorticity field (shown as contours). The velocity vectors are

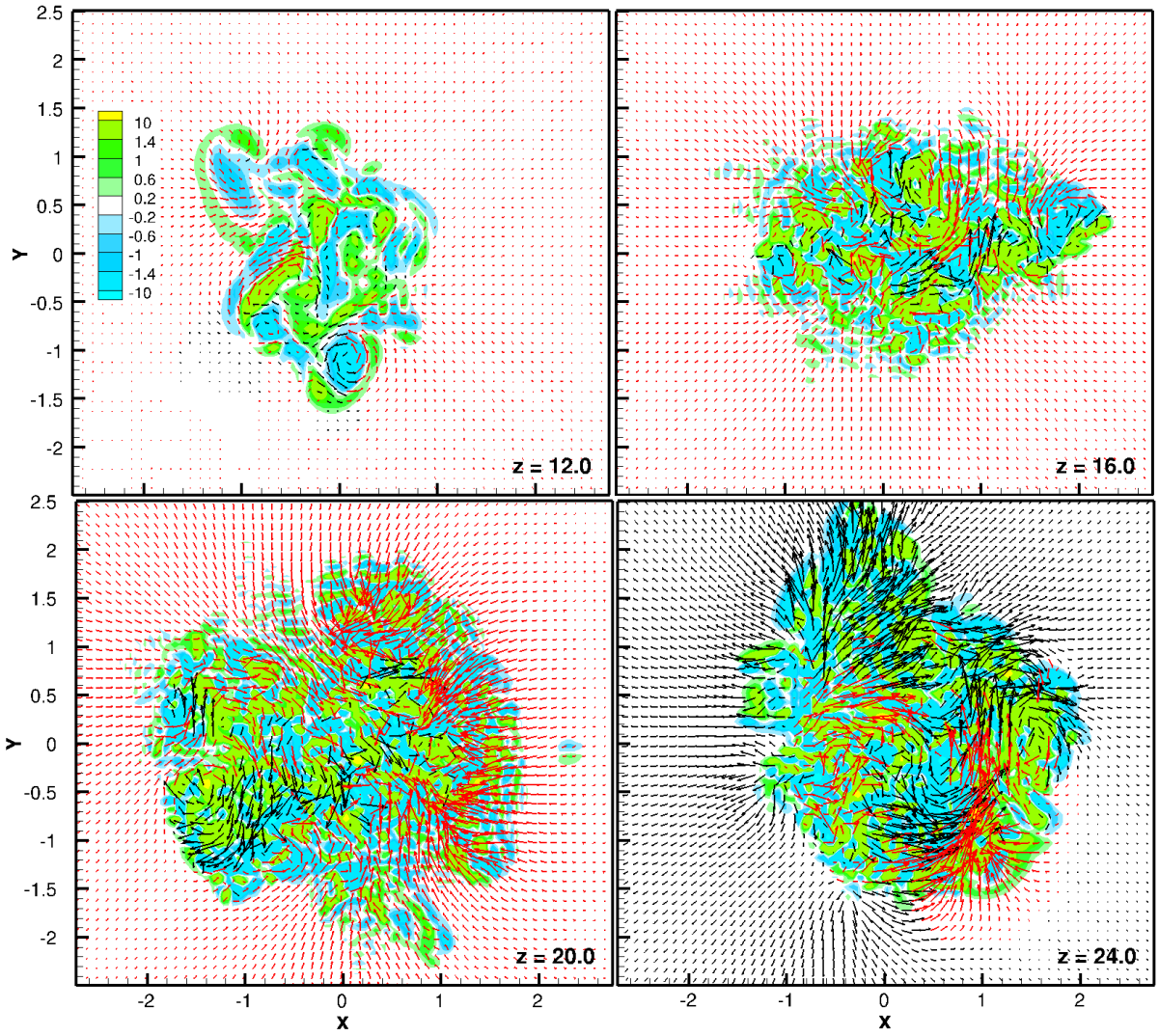

Figure 4.19: Diametral section of a diabatic plume at different axial distances. The contours represent axial vorticity field, inward velocity vectors are red and outward velocity vectors are black.

coloured black when the radial velocity is outward, and red when inward. Beyond HIZ the magnitude of the axial vorticity has increased significantly (by a factor of ≈ 5). The "entrainment tongues" (vortical structures) sticking out in the case of the non-diabatic plume are absent in the diabatic plume. The vorticity field is more comapct beyond HIZ and less organised than in the non-diabatic case. It can also be observed that post heat injection the contribution of small scale vorticity has increased significantly and this may be responsible for the crinkled edges of a cumulus cloud, as suggested by Narasimha (2012).

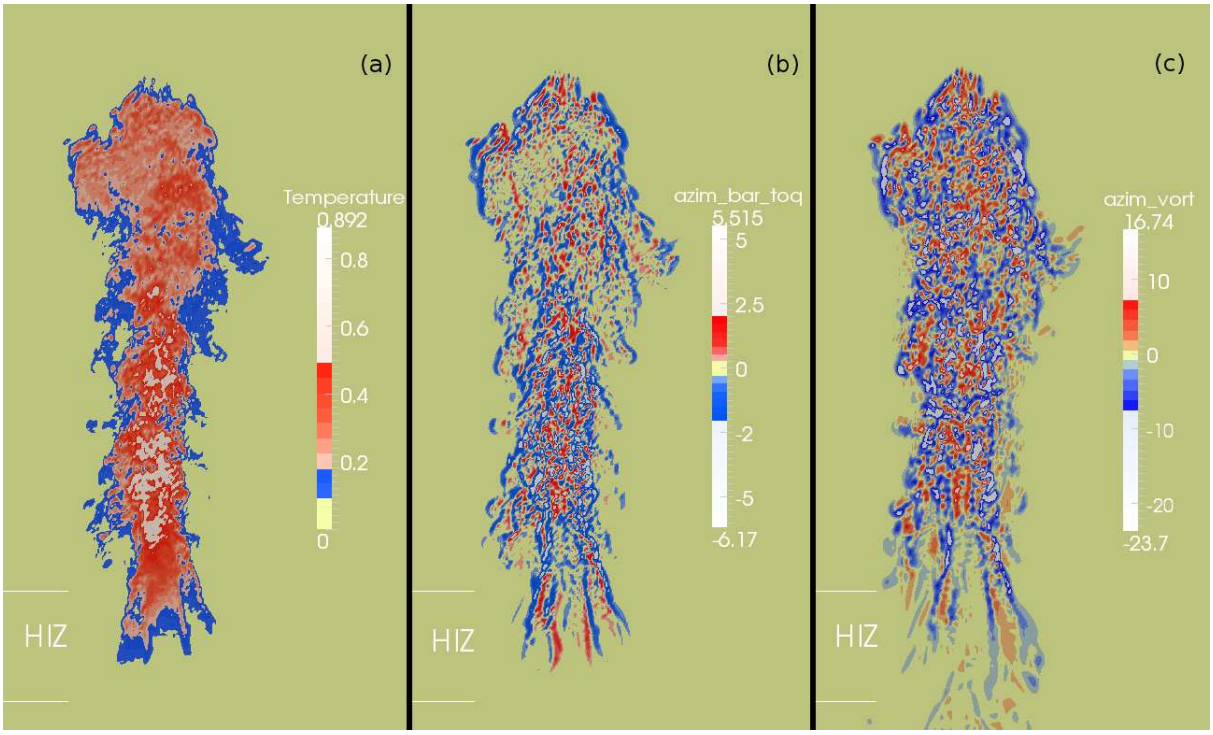

Figure 4.20: Axial section of a diabatic plume above the HIZ. (a) Temperature (b) Azimuthal component of baroclinic torque (c) Azimuthal vorticity

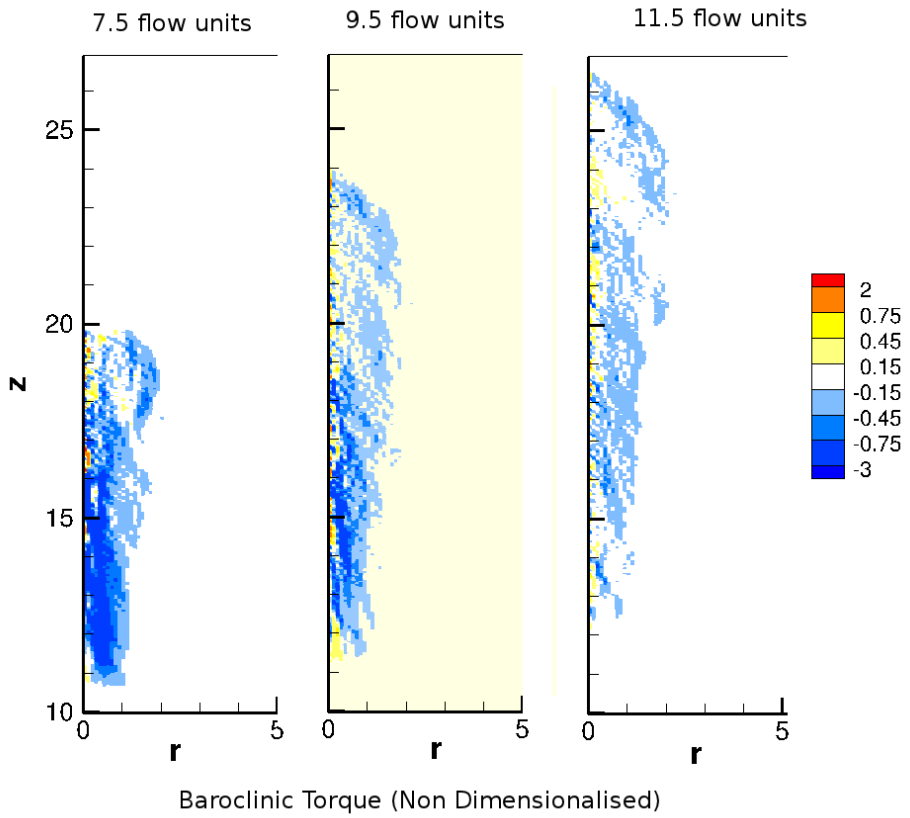

Figure 4.21: Axial section of a diabatic plume: Azimuthally averaged azimuthal component of baroclinic torque

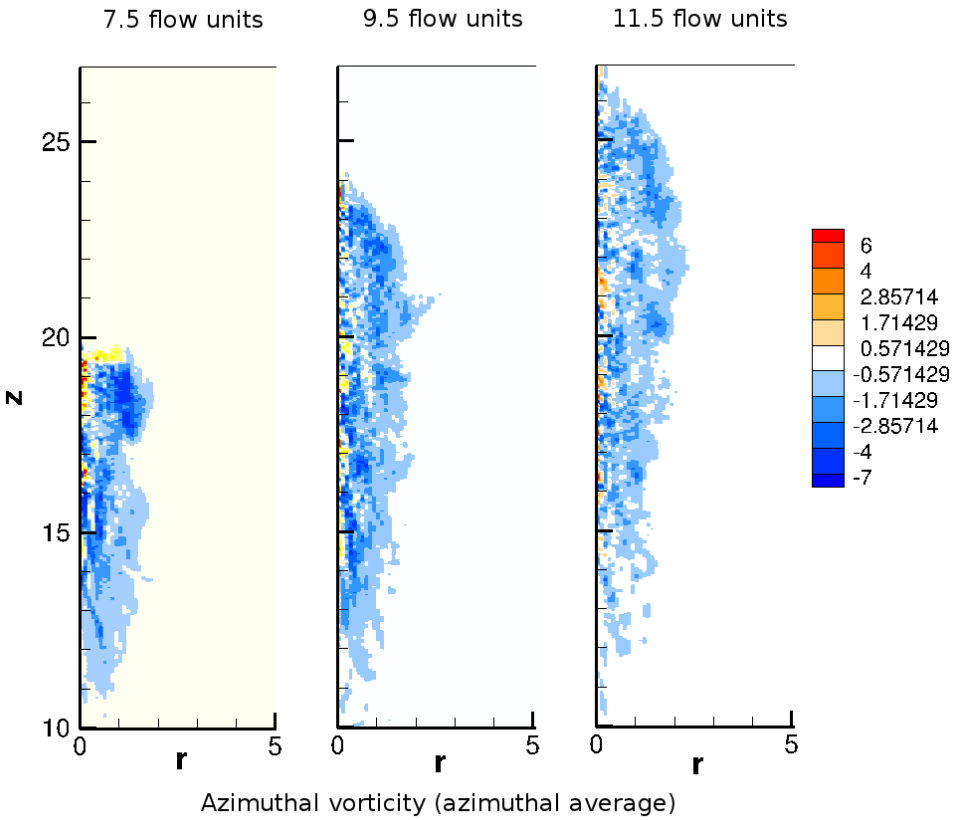

Figure 4.22: Axial section of a diabatic plume: Azimuthally averaged azimuthal vorticity

Figure 4.20 presents an axial section of a diabatic plume representing the temperature field, the azimuthal baroclinic torque and the azimuthal vorticity field. The azimuthal component of the baroclinic torque is representative of the variation of the buoyancy force in the radial direction, and contributes to the azimuthal component of the vorticity. It can be seen that the temperature gradients are strongest at some distance ($z \approx 16$) downstream from the HIZ. Close to the head the temperature gradients are small near the core. The core of the cloud flow is populated with high wavenumber azimuthal vorticity of both signs. It is in general difficult to make deductions from instantaneous flow field information, and since the flow considered here is inherently transient time averaging is not a viable option. The other option available is to perform ensemble averaging, but this has not been feasible atbpresent because of high computational costs. We exploit the axisymmetry of the flow field and perform azimuthal averages at a given instant in time.

Figures 4.21 and 4.22 present the radial variation of the azimuthally averaged value of azimuthal components of the baroclinic torque and vorticity respectively, at $t = 7.5$, 9.5 and 11.5. Both torque and vorticity are predominantly negative; there is hardly even a trace of positive torque or vorticity except near the axis. Close to the axis the presence of positive vorticity and torque maybe due to insufficient averaging because of the small

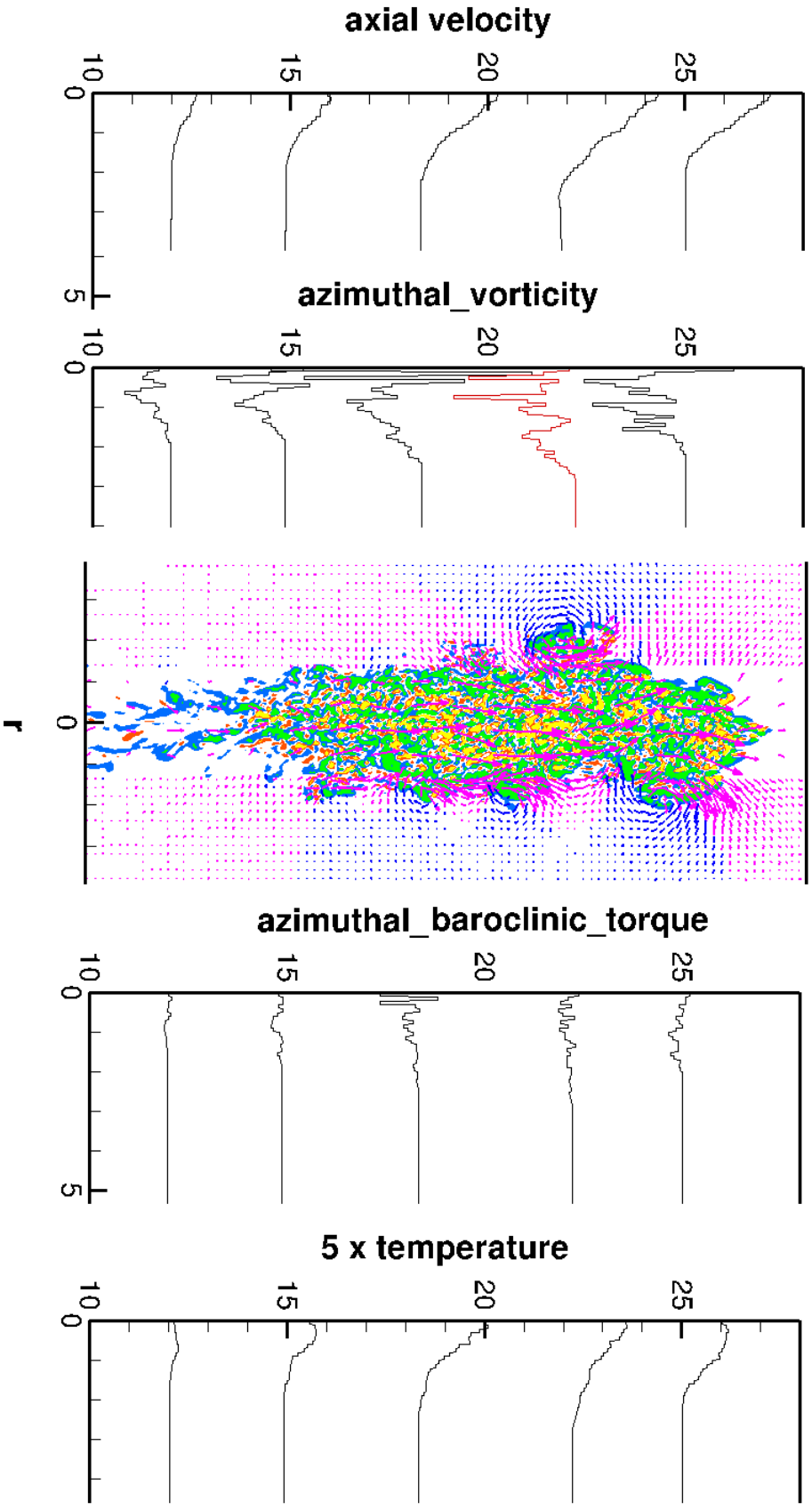

Figure 4.23: Diabatic plume: Axial velocity, azimuthal vorticity and baroclinic torque, 5 x temperature at different heights (azimuthally averaged)

number of grid points close to the axis. In figure 4.21 at $t = 7.5$ and $t = 9.5$ there is a concentration of negative torque (blue region) in a roughly tube-like structure near the heat injection zone; this is consistent with the idea proposed by Narasimha (2012). As we move downstream the contribution of baroclinic torque to azimuthal vorticity diminishes. On comparison between the average and instantaneous vorticty it can be observed that the fluctuating vorticity component is high, which implies that the fluctuating enstrophy which enhances mixing is also significantly high. This could be the reason for the well mixed cores in cumulus clouds. Figure 4.23 shows the radial variation of various averaged variables at different heights. The temperature profiles show off-axis peaks close to the HIZ and close to the cloud flow top. Similar observations were reported by Agrawal & Prasad (2004) in steady flows.

4.5 Entrainment

Entrainment is a key parameter in free shear flows. Following Morton *et al.* (1956) an entrainment coefficient α_E maybe defined by the relation

$$\frac{dm}{dz} = 2\pi b_u \alpha_E U_c \tag{4.1}$$

where b_u is a measure of the width of the flow, taken as the radial distance at which the azimuthally averaged axial velocity has fallen to e^{-1} of its centreline value. If the flow is self-similar α_E is a constant independent of z. In case of a cloud flow where the idea of self similarity is not applicable we define these scales based on the azimuthal averaged data set.

Figure 4.24 shows the variation of maximum axial velocity with axial distance. A cubic spline fit is used to smoothen out the fluctuations. The curve fit is shown in red. Within HIZ the fluctuations appear to be supressed, which may be attributed to the acceleration caused by heat release. Figure 4.25 presents the variation of mass flux in the axial direction. This mass flux is calculated by integrating across the diabatic plume to its edge defined by a threshold value based on vorticity magnitude. The closeness of the three curves based on thresholds varying by an order of magnitude (0.1 - 0.01) emphasises the sharpness of the edge. These variables along with the characteristic width shown in figure 4.26 are used to calculate the entrainment coefficient at a given instant for the cloud flow using equation 4.1. The variation of the entrainment coefficient with height is shown in figure 4.26.

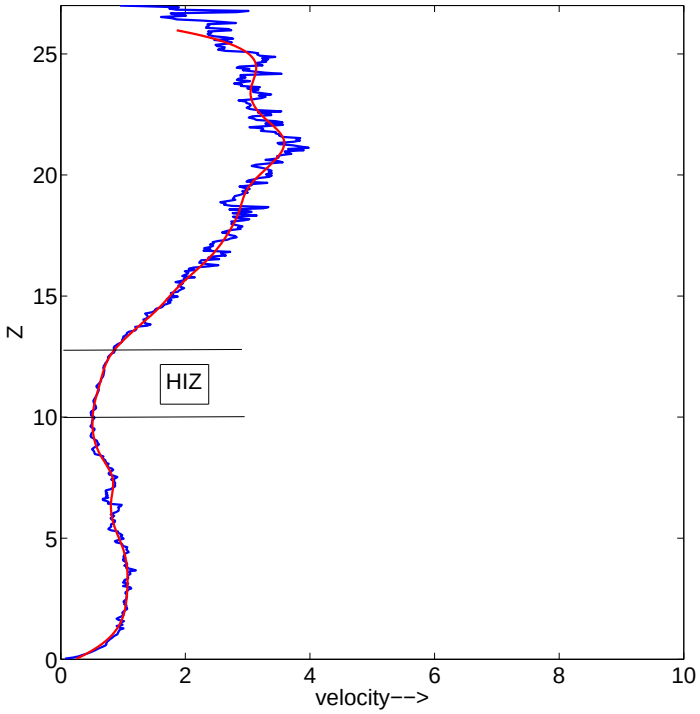

Figure 4.24: Variation of maximum axial velocity at different heights (blue), cubic spline fit (red)

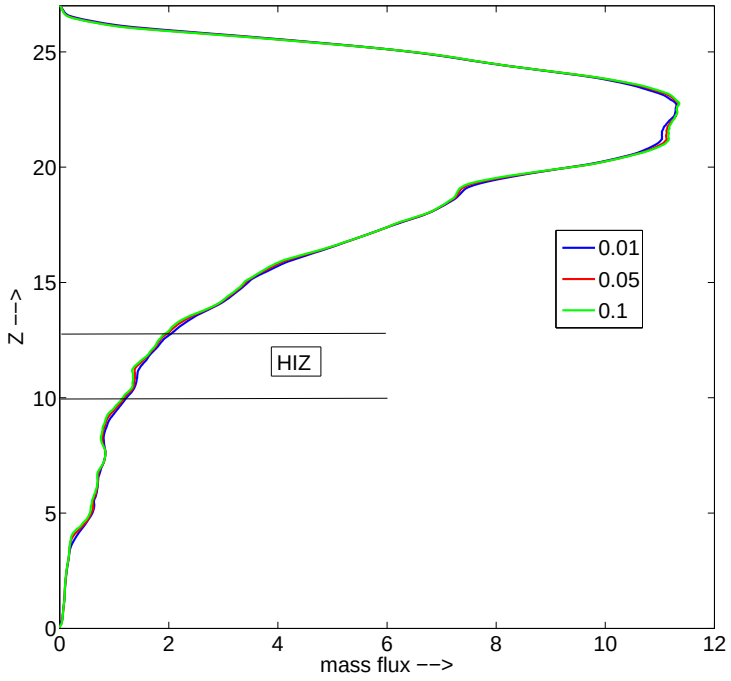

Figure 4.25: Variation of mass flux with height based on vortcity magnitude as threshold

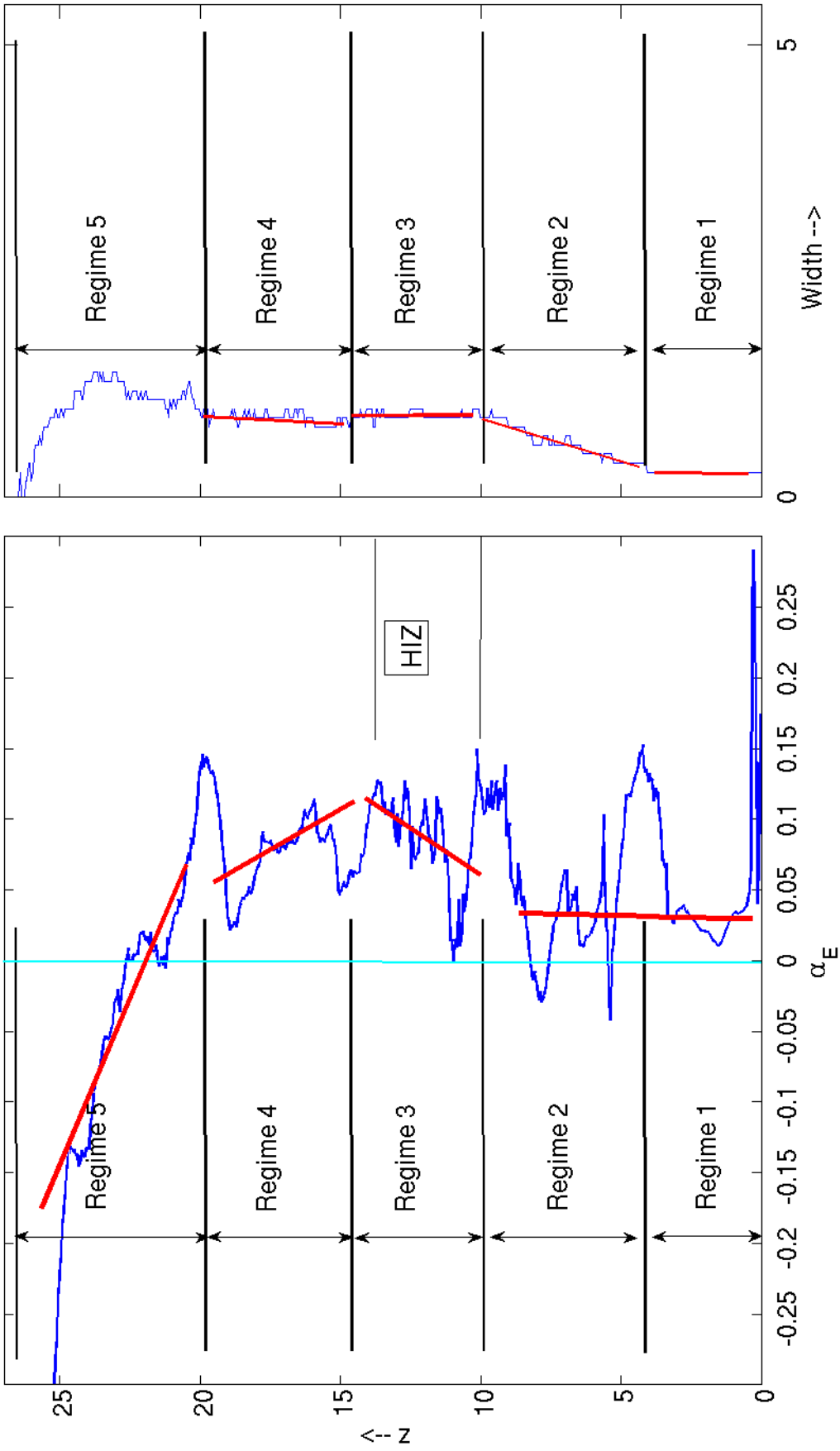

Figure 4.26: Variation of entrainment coefficient and width with height

The variation of the width of the flow with height shows 5 distinct regimes depicted in figure 4.26. In regime 1 the flow is laminar with constant width, followed by a nearly linearly spreading turbulent plume in regime 2. Regime 3 is essentially the HIZ, where the spread rate is arrested and the flow has a nearly constant width. In regime 4 a slow growth in width is observed, culminating at a maximum, in regime 5, which has a small dome or cloud head.

The entrainment coefficient obtained from this data set at a given instant has considerable statistical fluctuations. The red line drawn through this data is representative of a trend. α_E is constant in regime 1 and regime 2. Inside the HIZ (regime 3) there is an increase in the entrainment coefficient which peaks close to the end of regime 3. In regime 4 α_E decreases from its maximum value followed by a negative value in regime 5. The peaks in the fluctuating α_E curve are representative of the presence of strong local azimuthal/axial vorticity. For example figure 4.19, displaying the diametral section of the flow at $z = 20$, shows a strong entraining velocity field close to the edge in the diametral section, corresponding to the peak in the entrainment coefficient at $z \approx 20$.

Chapter 5
Conclusions and Future Work

In this thesis, we have developed and validated a 3D Navier-Stokes-Boussinesq solver based on kinetic energy conserving schemes capable of performing DNS of incompressible and Boussinesq flows. The solver so developed is used to perform a DNS of a transient diabatic plume to study the dynamics of cumulus cloud flows. The capability of the solver to simulate cloud-like flows has been shown by the flow visualisations presented from coarse grid ($\approx$ 4 million) simulations for various heating profiles. It is observed that the horizontal distribution of the heating profile also plays a significant role in determining the shape of any cumulus flow.

The effect of off-source heat addition on the vortical stuctures is clearly observed in the simulations using a resonably resolved ($\approx$ 129 million) grid. The breakdown of large scale structures into smaller scale structures is observed along with the folding down of the entrainment tongues. The effect of baroclinic torque on the flow field and the corresponding narrowing of the flow is captured. The observations reported here are consistent with the proposal made by Narasimha (2012). The organized vorticity field within the core may enhance entrainment or detarainment in different parts of the flow. The mass flux in the plume can be evaluated accuarately to a well-defined vorticity edge of the flow. Because of fluctuations, reliable estimates of the entrainment coefficient demand ensemble averages, which are left for future work. Further analysis is required to comment on the variation of the entrainment coefficient.

The highest resolution presented here (namely 129 million) for the cloud flow is not sufficient to resolve all the scales in the flow. So the resolution has to be improved further to get grid-independent results. The present solver is based on a second order accurate spatial discretisation. This can be improved to fourth order, thus helping to improve the accuracy of the results using a fewer grid points. We now have a reliable numerical code that can be used to simulate different cloud flows and obtain information about the entire flow field in a transient diabatic plume for the first time.

References

Agrawal, A., Boersma, B. & Prasad, A. K. 2005 Direct numerical simulation of a turbulent axisymmetric jet with buoyancy induced acceleration. *Flow, turbulence and combustion* **73** (3-4), 277–305.

Agrawal, A. & Prasad, A. K. 2004 Evolution of a turbulent jet subjected to volumetric heating. *Journal of Fluid Mechanics* **511**, 95–123.

Agrawal, A., Sreenivas, K. R. & Prasad, A. K. 2004 Velocity and temperature measurements in an axisymmetric turbulent jet with cloud-like off-source heating. *International journal of heat and mass transfer* **47** (6), 1433–1444.

Arakawa, A. 1966 Computational design for long-term numerical integration of the equations of fluid motion: Two-dimensional incompressible flow. part i. *Journal of Computational Physics* **1** (1), 119–143.

Babu, P. C. & Mahesh, K. 2004 Upstream entrainment in numerical simulations of spatially evolving round jets. *Physics of Fluids* **16**, 3699.

Basu, A. & Narasimha, R. 1999 Direct numerical simulation of turbulent flows with cloud-like off-source heating. *Journal of Fluid Mechanics* **385** (1), 199–228.

Bhat, G., Narasimha, R. & Arakeri, V. 1989 A new method of producing local enhancement of buoyancy in liquid flows. *Experiments in fluids* **7** (2), 99–102.

Bhat, G. S. & Narasimha, R. 1996 A volumetrically heated jet: large-eddy structure and entrainment characteristics. *J. Fluid Mech.* **325**, 303–330.

Biringen, S. & Peltier, L. 1990 Numerical simulation of 3-d bénard convection with gravitational modulation. *Physics of Fluids A: Fluid Dynamics* **2**, 754.

Bisset, D. K., Hunt, J. C. & Rogers, M. M. 2002 The turbulent/non-turbulent interface bounding a far wake. *Journal of Fluid Mechanics* **451**, 383–410.

Blyth, A. M. 1993 Entrainment in cumulus clouds. *Journal of applied meteorology* **32** (4), 626–641.

Boersma, B., Brethouwer, G. & Nieuwstadt, F. 1998 A numerical investigation on the effect of the inflow conditions on the self-similar region of a round jet. *Physics of fluids* **10**, 899.

Brown, Garry, L. & Roshko, A. 1974 On density effects and large structure in turbulent mixing layers. *Journal of Fluid Mechanics* **64** (4), 775–816.

Byers, H. R. & Braham, R. R. 1949 *The thunderstorm: report of the Thunderstorm Project*. US Government Printing Office.

Charney, J. G. & Shukla., J. 1981 Cambridge University Press.

Chorin, A. J. 1968 Numerical solution of the navier-stokes equations. *Mathematics of computation* **22**, 745–762.

Corrsin, S. & Kistler, A. L. 1955 Free-stream boundaries of turbulent flows.

De Rooy, W. C. & Siebesma, A. P. 2008 A simple parameterization for detrainment in shallow cumulus. *Monthly Weather Review* **136** (2), 560–576.

Deshpande, M. & Shankar, P. 1994 Direct numerical simulation of a complex turbulent flow. *Current Science* **66** (10), 767–770.

Diwan, S. S., Narasimha, R., Bhat, G. S. & Sreenivas, K. R. 2011 Laboratory studies of anomalous entrainment in cumulus cloud flows. In *Journal of Physics: Conference Series*, , vol. 318, p. 072014. IOP Publishing.

Erturk, E. 2009 Discussions on driven cavity flow. *International journal for numerical methods in fluids* **60** (3), 275–294.

Falgout, R. D., Jones, J. E. & Yang, U. M. 2006 The design and implementation of hypre, a library of parallel high performance preconditioners. In *Numerical solution of partial differential equations on parallel computers*, pp. 267–294. Springer.

Herrmann, M., Blanquart, G. & Raman, V. 2004 Flux corrected finite-volume scheme for preserving scalar boundedness in large-eddy simulations. *Annu. Res. Briefs* **2004**, 75–85.

Heus, T. & Jonker, H. J. 2008 Subsiding shells around shallow cumulus clouds. *Journal of the Atmospheric Sciences* **65** (3), 1003–1018.

Heymsfield, A. J., Johnson, P. N. & Dye, J. E. 1978 Observations of moist adiabatic ascent in northeast colorado cumulus congestus clouds. *Journal of the Atmospheric Sciences* **35** (9), 1689–1703.

Houze Jr, R. A. 1994 *Cloud dynamics*, , vol. 53. Access Online via Elsevier.

Hussein, H. J., Capp, S. P. & George, W. K. 1994 Velocity measurements in a high-reynolds-number, momentum-conserving, axisymmetric, turbulent jet. *Journal of Fluid Mechanics* **258** (1), 31–75.

Jonker, H. J., Heus, T. & Sullivan, P. P. 2008 A refined view of vertical mass transport by cumulus convection. *Geophysical Research Letters* **35** (7).

Konduri, A. 2009 Direct numerical simulations of starting-plume cloud-flows. Master's thesis, Jawaharlal Nehru Centre for Advanced Scientific Research, Bangalore.

Ku, H. C., Hirsh, R. S. & Taylor, T. D. 1987 A pseudospectral method for solution of the three-dimensional incompressible navier-stokes equations. *Journal of Computational Physics* **70** (2), 439–462.

Lipps, F. B. 1976 Numerical simulation of three-dimensional bénard convection in air. *Journal of Fluid Mechanics* **75** (01), 113–148.

Ludlam, F. H., Scorer, R. S. *et al.* 1957 Cloud study. a pictorial guide. *Cloud study. A pictorial guide.* .

Mahesh, K., Constantinescu, G. & Moin, P. 2004 A numerical method for large-eddy simulation in complex geometries. *Journal of Computational Physics* **197** (1), 215–240.

Mathew, J. & Basu, A. J. 2002 Some characteristics of entrainment at a cylindrical turbulence boundary. *Physics of Fluids* **14**, 2065.

Moin, P. & Mahesh, K. 1998 Direct numerical simulation: a tool in turbulence research. *Annual Review of Fluid Mechanics* **30** (1), 539–578.

Morinishi, Y., Lund, T., Vasilyev, O. & Moin, P. 1998 Fully conservative higher order finite difference schemes for incompressible flow. *Journal of Computational Physics* **143** (1), 90–124.

Morton, B., Taylor, G. & Turner, J. 1956 Turbulent gravitational convection from maintained and instantaneous sources. *Proceedings of the Royal Society of London. Series A. Mathematical and Physical Sciences* **234** (1196), 1–23.

Muppidi, S. & Mahesh, K. 2008 Direct numerical simulation of passive scalar transport in transverse jets. *Journal of Fluid Mechanics* **598**, 335–360.

Narasimha, R. 2012 Cumulus clouds and convective boundary layers: a tropical perspective on two turbulent shear flows. *Journal of Turbulence* (13).

Narasimha, R., Diwan, S. S., Duvvuri, S., Sreenivas, K. R. & Bhat, G. S. 2011 Laboratory simulations show diabatic heating drives cumulus-cloud evolution and entrainment. *Proceedings of the National Academy of Science* .

Paluch, I. R. 1979 The entrainment mechanism in colorado cumuli. *J. Atmos.sci.* **36** (12), 2467–2478.

Panchapakesan, N. & Lumley, J. 1993 Turbulence measurements in axisymmetric jets of air and helium. part 1. air jet. *Journal of Fluid Mechanics* **246** (1), 197–223.

ParaView, G. 2008 Version 3.0 kitware, inc.

Pauluis, O. & Schumacher, J. 2011 Self-aggregation of clouds in conditionally unstable moist convection. *Proceedings of the National Academy of Sciences* **108** (31), 12623–12628.

Perot, J. B. 1993 An analysis of the fractional step method. *Journal of Computational Physics* **108** (1), 51–58.

Ramaswamy, V., Boucher, O., Haigh, J., Hauglustaine, D., Haywood, J., Myhre, G., Nakajima, T., Shi, G. & Solomon, S. 2001 Climate change 2001: The scientific basis. *Contribution of working group I to the Third Assessment Report of the Intergovernmental Panel on Climate Change* **8510**.

Randall, D. A., Wood, R. A., Bony, S., Colman, R., Fichefet, T., Fyfe, J., Kattsov, V., Pitman, A., Shukla, J., Srinivasan, J. *et al.* 2007 Climate models and their evaluation. *Tech. Rep.*.

Reuter, G. W. 1986 A historical review of cumulus entrainment studies. *Bulletin of the American Meteorological Society* **67** (2), 151–154.

Riehl, H. & Malkus, J. S. 1958 On the heat balance in the equatorial trough zone. *Geophysica* **6** (3-4), 503–538.

Romps, D. M. & Kuang, Z. 2010 Do undiluted convective plumes exist in the upper tropical troposphere? *Journal of the Atmospheric Sciences* **67** (2), 468–484.

de Rooy, W. C., Bechtold, P., Fröhlich, K., Hohenegger, C., Jonker, H., Mironov, D., Pier Siebesma, A., Teixeira, J. & Yano, J.-I. 2012 Entrainment and detrainment in cumulus convection: an overview. *Quarterly Journal of the Royal Meteorological Society* .

Sani, R. L. & Gresho, P. M. 1994 Resume and remarks on the open boundary condition minisymposium. *International Journal for Numerical Methods in Fluids* **18** (10), 983–1008.

Siebesma, A. & Cuijpers, J. 1995 Evaluation of parametric assumptions for shallow cumulus convection. *Journal of the Atmospheric Sciences* **52** (6), 650–666.

Sloss, P. W. 1967 An empirical examination of cumulus entrainment. *Journal of Applied Meteorology* **6**, 878–881.

Spiegel, E. & Veronis, G. 1960 On the boussinesq approximation for a compressible fluid. *The Astrophysical Journal* **131**, 442.

Squires, P. 1958 Penetrative downdraughts in cumuli. *Tellus* **10** (3), 381–389.

Starr Malkus, J. 1954 Some results of a trade-cumulus cloud investigation. *Journal of Meteorology* **11** (3), 220–237.

Stommel, H. 1947 Entrainment of air into a cumulus cloud: (paper presented 27 december 1946 at the annual meeting, ams, cambridge, massachusetts). *Journal of Meteorology* **4** (3), 91–94.

Taylor, G. 1946 *Dynamics of a mass of hot gas rising in air*. Technical Information Division, Oak Ridge Operations.

Temam, R. 1969 Sur lapproximation de la solution des equations de navier stokes par le methode des. *Arch. Rat. Mech. Anal* **33**, 377–385.

Turner, J. 1963 Model experiments relating to thermals with increasing buoyancy. *Quarterly Journal of the Royal Meteorological Society* **89** (379), 62–74.

Turner, J. 1983 S. 1973 buoyancy effects in fluids.

Venkatakrishnan, L., Bhat, G., Prabhu, A. & Narasimha, R. 1998 Visualization studies of cloud-like flows. *Current Science* **74** (7), 597–606.

Venkatakrishnan, L., Elavarasan, R., Bhat, G., Krothapalli, A. & Lourenco, L. 2003 Particle image velocimetry study of a cloud-like flow. *Current Science* **85** (6), 778–785.

Verstappen, R. & Veldman, A. 2002 Symmetry-preserving discretization of turbulent channel flow. In *High Performance Scientific and Engineering Computing*, pp. 107–114. Springer.

Warhaft, Z. 2009 Laboratory studies of droplets in turbulence: towards understanding the formation of clouds. *Fluid Dynamics Research* **41** (1).

Warner, J. 1955 The water content of cumuliform cloud. *Tellus* **7** (4), 449–457.

WMO 1975 International cloud atlas. *World Meteorological Organization.* **1**.